Active Acoustic Emission from a Two-dimensional Electron Gas

by

Lei Shao

A dissertation submitted in partial fulfillment
of the requirements for the degree of
Doctor of Philosophy
(Mechanical Engineering)
in the University of Michigan
2014

Doctoral Committee:

Associate Professor Kevin P. Pipe, Chair
Professor Pallab Bhattacharya
Professor Karl Grosh
Professor Katsuo Kurabayashi

© Lei Shao 2014

This dissertation is dedicated to my wife, Wenjie Xu.

Acknowledgements

This work represents a cumulation of the time and effort of a number of people. Here I would like to highlight those whom I feel deserve special recognition.

First of all, I am deeply grateful to my adviser Kevin Pipe. Kevin is incredibly supportive during my PhD study. His knowledge base, creativity, and positive attitude have made my stay in his group an enjoyable and rewarding one and have made a lasting impact on my future endeavors. He is the one who told me that there are many ups and downs during one's PhD study when my first conference abstract was denied. And he is the first one who told me that I was doing a great job even when I only made a very small achievement. Kevin constantly impressed me also by his skill of quickly grasping the key ideas behind unfamiliar and difficult terminologies and then precisely rephrasing it in a plain language so that a non-scientist can easily understand. I have been paying close attention to develop this skill and perhaps this is the one of the most important qualities I learned from Kevin.

I am indebted also to Meng Zhang. Meng is the most important collaborator of this work and he is also my mentor in the Lurie Nanofabrication Facility (LNF). By performing molecular beam epitaxy technique in his spare time, he grew GaN based

epitaxial structures on several sapphire wafers which were used for most part of this work. He also taught me a lot of microfabrication skills in the LNF, from drawing photomasks by using a CAD software to detailed photolithography skills.

I would like to thank other members of my thesis committee, Pallab Bhattacharya for his help for GaN epitaxy growth, Karl Grosh for many inspiring discussions about acoustic waves, and Katsuo Kurabayashi for his technical guidance and time from my qualification exam to my final defense. Defense Advanced Research Projects Agency (DARPA) also deserves acknowledgement for funding my research.

Being in the Pipe Research Group for a little over 4 years, I would like to thank many lab members as well, Abhishek Yadav for his cold humor and cheer, Huarui Sun for his attitude, discussions on acoustics and help with measurement setups, Yansha Jin for her warmth, Gun Ho Kim for his reason, collaborations, intelligence and numerous sparking discussions, Kejia Zhang for her collaborations and intelligence, Si Hui for his ideas and help both inside and outside the lab, and Vahid Rashidi for his humor and laugh.

There are also many friends and colleagues during my nearly 4 years' experience in the LNF. First I would like to highlight Azadeh Ansari for her time to teach me on RF resonators, Vikrant Gokhale for his help with GaN etching, Cheng Zhang for his knowledge in thin film thickness characterization, and Yuchao Yang for his small but useful fabrication skills. I would also like to thank Nadine Wang, Sandrine Martin, Pilar Herrera-Fierro, Steven Sostrom, Gregory Allion, Kevin Owen, Wenbing Hu, Animsh Banerjee, Sishir Bhowmick, Shafat Jahangir, Siddharth Gaba, Che-Hung Liu, Kyunghoon Lee, Tao Ling, Ning Wang, and Dewei Zhao.

Having been at Ann Arbor for nearly 5 years, I have made many friends who made my stay here filled with cheer. In particular, I would like to thank Yijun Fan and Bo Liu as my groomsmen, Hanxiao Wang and Lingli He as the witnesses of my civil ceremony, and Chenjun Wei as my first roommate back in 2009. I would also like to thank Yifeng Tang, Yan Zhai, Yunjiao Cai, Qinling Shen, Ning Wang, Jialiang Yan, Keqin Cao, Jun Liu, Xianke Lin, and Bo Yu.

My most heartfelt gratitude is reserved for my family, which has always been a source of great support, courage and strength. Without constant love from my parents and parents-in-law, I cannot imagine going through the whole PhD process myself. I can feel how much they care about me from their prayers, their willingness to take the long journey to visit here, and our numerous video chats about life and research in Michigan. My particular gratitude goes to my mom-in-law for her help with cooking and housework during the last several months of my PhD study. Finally, I would thank Heaven for bringing my wife, Wenjie Xu, into my life. Words cannot express the unwavering love and support from her during my PhD study. Knowing that I will have the rest of my life to spend with her since our wedding ceremony on August 18th 2012 is truly joyful.

Table of Contents

Dedication .... **ii**

Acknowledgements .... **iii**

List of Figures .... **viii**

Abstract .... **xiii**

1 Background **1**

1.1 Piezoelectricity and Acoustic Wave Devices 1

1.2 Gallium Nitride Based Two-dimensional Electron Gas 7

1.3 Active Acoustic Emitter Based on a 2DEG 10

2 Emission and Detection of SAWs by a 2DEG **15**

2.1 Previous Work 15

2.2 Device Design and Fabrication 17

2.3 Acoustic Emission from a 2DEG 20

2.3.1 Source-Gate Modulation 21

2.3.2 Source-Drain Modulation 26

2.4 Acoustic Detection by a 2DEG 27

2.5 Conclusion 31

3 Active Control of SAW Emission **32**

3.1 Field Modulation in a HEMT 32

3.2 Optical Reflectance Spectroscopy 39

3.3 SAW Mode Switching 42
3.3.1 Mode Dynamics in an Interdigital Transducer 42
3.3.2 Multi-gate HEMT 42
3.3.3 Single-gate HEMT 46
3.4 Conclusion 49
4 Coupling of SAWs and Drifting Electrons in a 2DEG 50
4.1 Conventional Acoustoelectric Theory and Applications 51
4.2 Amplification of Acoustic Waves by a Biased 2DEG 53
4.3 Characterizing Directional Emission of SAWs 60
4.4 Conclusion 67
5 Conclusion and Future Work 68
5.1 Future Work: Nondestructive Ultrasonic Diagnostics of HEMTs 69
5.2 Future Work: 2DEG Transducers 70
5.2.1 GaN 2DEG-based Nanomechanical Resonators 71
5.2.2 GaN 2DEG-based Ultra-sensitive Bio-detectors 73
5.3 Pulsed Laser Interferometer 77
Bibliography 81

List of Figures

Figure 1-1: Change in charge distribution of a quartz network under mechanical stress. Blue circles refer to silicon atoms and red circles refer to oxygen atoms [1]. 2

Figure 1-2: Side view of a thin-film bulk acoustic resonator. 3

Figure 1-3: Excitation of surface acoustic waves by a coupling wedge. 4

Figure 1-4: Top view of an interdigital transducer fabricated on a piezoelectric substrate for surface acoustic wave emission [2]. 5

Figure 1-5: An IDT-to-IDT pair leads to numerous applications in various fields. 5

Figure 1-6: Various applications of surface acoustic waves (SAWs)................................ 6

Figure 1-7: Crystal structure of GaN and the built-in polarization vector......................... 8

Figure 1-8: A conventional AlGaN/GaN high electron mobility transistor structure. The dotted line indicates the 2DEG channel that connects the source and drain. 9

Figure 1-9: Built-in tensile strain in AlGaN layer due to lattice mismatch. 9

Figure 1-10: SAW modes supported by a GaN-on-sapphire structure. 11

Figure 2-1: Integrated HEMT-IDT structure. 18

Figure 2-2: Design of the epitaxial layer structure. 18

Figure 2-3: Micro-fabrication process of the integrated HEMT-IDT structure................ 19

Figure 2-4: Optical images of the fabricated HEMT-IDT structure and three different designs of IDTs, indicated as (a), (b) and (c)... 20

Figure 2-5: Setup for characterization of the HEMT-IDT transmission while the RF signal is applied to the V_{GS}. 22

Figure 2-6: IDT-IDT transmission and HEMT-IDT transmission when the RF signal is applied across and source-gate electrodes. 23

Figure 2-7: HEMT DC characteristics and bias point in Figure 2-6b.............................. 24

Figure 2-8: Amplitude of SAW peak as a function of VDS and the DC component of V_{GS}. 24

Figure 2-9: Characterization of the HEMT-IDT transmission while the RF signal is applied across the source-drain electrodes... 27

Figure 2-10: Detection of incident SAWs by a 2DEG. 28

Figure 2-11: IDT-IDT transmission and IDT-HEMT transmission in which the HEMT is operated at the DC bias point shown in the inset.. 29

Figure 2-12: AC admittance under various HEMT operation conditions........................ 30

Figure 3-1: Potential distribution in a GaN/AlGaN heterostructure in which the 2DEG is depleted. 34

Figure 3-2: Transconductance of the simulated HEMT and DC-dependent electrical fields at two depths in the simulated epitaxy for the case in which the 2DEG is depleted. 35

Figure 3-3: Potential distribution in a GaN/AlGaN heterostructure in which the 2DEG is present. 36

Figure 3-4: Transconductance of the simulated HEMT and DC-dependent electrical fields at two depths in the simulated epitaxy for the case in which the 2DEG is present. 37

Figure 3-5: Optical reflectance spectroscopy setup used to measure ΔR/R (SAW amplitude) vs. bias frequency. 40

Figure 3-6: SAW spectrum emitted from an IDT under DC bias at 0V and -4V. 41

Figure 3-7: DC dependences of each resonant mode including R, L, PB1 and PB2. 41

Figure 3-8: Characterization of the SAW emission spectrum of a 4-gate transistor and the DC dependences of the four primary acoustic modes (R, L, PB1 and PB2). 43

Figure 3-9: Calculated vertical strain modulation induced in the 2DEG by carrier density modulation, as a function of $V_{GS,DC}$, as well as the calculated vertical strain modulation induced by IDTs of three different sizes. 46

Figure 3-10: Characterization of the SAWs emitted by a single-gate HEMT. (a) DC characteristics of the 1-gate transistor. (b) Transconductance of the 1-gate transistor with V_{DS} set at 10 V. (c) DC dependences of the amplitudes of the four SAW modes emitted from the 2DEG as a function of $V_{GS,DC}$ when V_{DS} is set at 10 V. (d)–(h) Acoustic spectra when $V_{GS,DC}$ is set at 2 V and V_{DS} is increased in 2 V increments from 4 V to 12 V, as illustrated by the red dots and arrow in (a). 48

Figure 4-1: Illustration of a layer structure and applied bias supporting SAW amplification. 55

Figure 4-2: SAW power gain per unit length of interaction with a DC biased 2DEG, as a function of electron velocity for four different values of 2DEG carrier density. 57

Figure 4-3: Gain per unit length as a function of 2DEG density for four different values of electron velocity, based on the same condition used in Figure 4-2. 57

Figure 4-4: Solid curves: gain per SAW wavelength for the four different values of 2DEG density used in Figure 4-2, assuming an electron drift velocity of 3×10^6 cm/s; dashed curves: gain per SAW wavelength if electron diffusion is ignored by setting Λ to zero.. 58

Figure 4-5: Comparison of the interaction strength for SAWs and drifting electrons in a GaN-based 2DEG and bulk GaN at equivalent carrier densities. 60

Figure 4-6: A HEMT on an AlGaN/GaN 2DEG structure is used as an active SAW emitter with directional emission functionality under certain bias conditions. S stands for source, G for gate, and D for drain. 61

Figure 4-7: Calculated ratio of the SAW power emitted from the drain side to that from the source side as a function of electron velocity for four different values of 2DEG density. 62

Figure 4-8: HEMT's transconductance and source-drain current (I_{DS}) as a function of V_{DS} and $V_{GS,DC}$, with V_{DS} held at 1 V. 63

Figure 4-9: SAW power emitted at 0.8 GHz from the drain side (black) and source side (gray), as a function of $V_{GS,DC}$, with V_{DS} held at 1 V. The power is normalized to the minimum measured at $V_{GS,DC}$ = -2 V; the emission ratio (drain/source) is shown in magenta. 64

Figure 4-10: (a) and (b) SAW power emitted from the drain side and source side as a function of V_{DS}, with $V_{GS,DC}$ held at -1.55 V and -0.80 V, respectively. 65

Figure 4-11: SAW power ratio (drain/source) as a function of V_{DS}, with $V_{GS,DC}$ varied from -1.60 V to -1.45 V with a step size of 0.05 V (points). Also shown are predicted power ratios for which the electron velocity in Figure 4-7 is converted to V_{DS} by assuming a constant 2DEG mobility (lines). 66

Figure 5-2: High electron mobility resonant body transistor. Dashed lines represent the 2DEG at the AlGaN/GaN interface. 72

Figure 5-3: (a) Conventional AlGaN/GaN HEMT design. (b) Design of an InAlN/GaN HEMT based biosensor with a specially functionalized gate. 75

Figure 5-4: Vision for all-GaN-based biomedical and chemical sensing microsystems. . 76

Figure 5-5: Stroboscopic Michelson interferometer (PD, photodiode). The beam path is indicated by red lines, while electrical connections are indicated by black dotted lines. . 79

Abstract

This work examines the performance and fundamental operating principles of an active acoustic emitter based on an AlGaN/GaN high electron mobility transistor (HEMT). Strong piezoelectric effects in GaN-based semiconductors enable the formation of a two-dimensional electron gas (2DEG) that acts as the HEMT channel. Because of the strong coupling between 2DEG carrier density and mechanical deformation, HEMTs offer methods for active control of acoustic emission that are not possible with traditional passive emitters.

First it is shown that intense surface acoustic waves (SAWs) are generated when the gate-source voltage is modulated at a high frequency that is resonant with the transistor geometry, due to the dynamic screening of the built-in strain in the AlGaN layer by the modulated 2DEG carrier density. The dynamic strain modulation generated during typical RF operation of an AlGaN/GaN based 2DEG is found to be two to three orders of magnitude higher than that generated by a conventional SAW emitter (interdigital transducer) at a similar size under the same RF operation.

Next it is shown that the gate-source DC bias, which controls whether modulation occurs about a bias point at which the 2DEG is depleted or present, can be used to select the particular acoustic mode emitted.

Finally it is shown that the drain-source DC bias can be used to control the directionality of acoustic emission through acoustoelectric amplification (or attenuation) of acoustic waves traveling in the same (or opposite) direction as the 2DEG electron drift current. In a measured HEMT, when an RF signal is applied across the gate/source electrodes to effect SAW generation in the presence of a DC bias across the drain/source, the ratio of SAW power emitted from the drain side to that from the source side reaches approximately 1.6 due to this effect.

Chapter 1

Background

Acoustic wave devices such as interdigital transducers, thin-film bulk acoustic resonators, and acoustic wedge transducers have been widely used in imaging, sensing, actuating, and signal processing. These devices rely on the piezoelectric effect, which leads to mechanical deformation in response to an applied electric field, or an electric field in response to mechanical strain. While conventional acoustic wave devices are passive and operate on insulating piezoelectric dielectric substrates, two-dimensional electron gases (2DEGs) formed at interfaces of piezoelectric semiconductors provide intense coupling between electric charge and mechanical strain over nanometer distances. Active devices utilizing 2DEGs, such as high electron mobility transistors (HEMTs), offer new means to control acoustic emission in terms of intensity, frequency response, and emission pattern.

1.1 Piezoelectricity and Acoustic Wave Devices

Piezoelectricity was discovered by Jacques and Pierre Curie in 1880 during studies on quartz crystals [3]. When piezoelectric materials are mechanically deformed, their

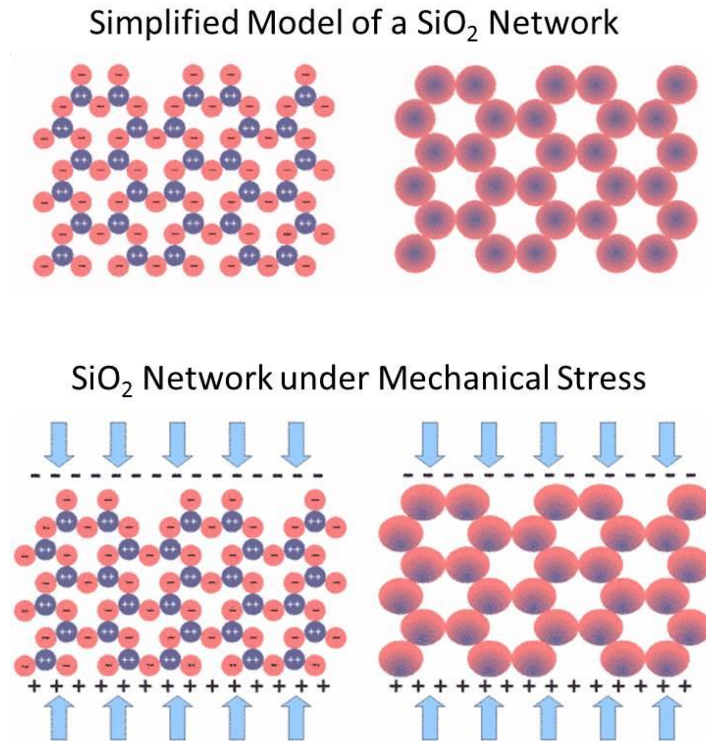

Figure 1-1: Change in charge distribution of a quartz network under mechanical stress. Blue circles refer to silicon atoms and red circles refer to oxygen atoms [1].

surfaces become electrically charged (see quartz as an example in Figure 1-1). The reverse is also true: the same materials will become deformed when put into an electric field. The origin of piezoelectricity is the built-in polarization in certain crystal structures [4] of materials such as quartz, zinc oxide (ZnO), aluminum nitride (AlN), lead zirconate titanate (PZT), lithium niobate ($LiNbO_3$), gallium arsenide (GaAs), Lithium Tantalate ($LiTaO_3$), etc.

Due to the ease of transduction between mechanical and electrical domains, piezoelectric materials are widely used in many applications such as actuators, high voltage sources and mechanical sensors. Numerous industrial and manufacturing markets

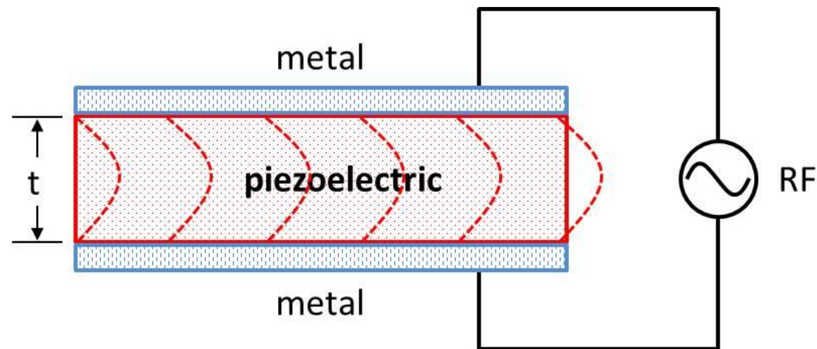

Figure 1-2: Side view of a thin-film bulk acoustic resonator.

currently exist for piezoelectric devices, including the automotive industry. Strong demand also comes from medical instruments for imaging as well as information and telecommunication devices such as cellular phones, laptops, and printers [5]. The 2013 global market for piezoelectric actuators and motors alone was valued at approximately $11.1 billion, and this market is estimated to reach $16 billion by 2018 [6].

One of the important uses of piezoelectric materials is as a means to generate acoustic waves in a solid, in particular, bulk acoustic waves (BAWs) and surface acoustic waves (SAWs). BAWs are usually excited by a device called a film bulk acoustic-wave resonator (FBAR) [7], which is composed of a piezoelectric film sandwiched between two metal contacts (see Figure 1-2). Longitudinal waves can be easily generated when an oscillating field is applied across the FBAR. The resonant frequency of the fundamental mode is $F_{res} = V_a/(2t)$, where V_a is the acoustic velocity in the direction of emission and t is the thickness of the piezoelectric film.

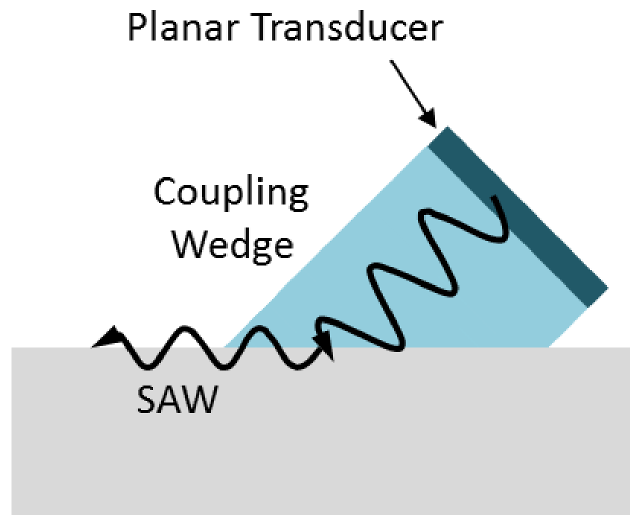

Figure 1-3: Excitation of surface acoustic waves by a coupling wedge.

SAWs are elastic waves travelling on the surface of a solid, and thus are externally accessible during propagation, making them more convenient for numerous applications. Prior to the 1960s, SAWs were excited by a wedge transducer (see Figure 1-3), which couples BAWs onto the surface of a solid [8].

In 1965, White and Voltmer invented an efficient SAW transducer composed of two interdigital combs of electrodes (see Figure 1-4), now commonly known as interdigital transducers (IDTs) [9]. The wavelength of the emitted SAW is determined by the spacing of the electrodes (*d*), and thus the center frequency is $F_{res} = V_a / d$.

Soon after, researchers realized that two identical IDTs could be used as a pair (see Figure 1-5) in which the left IDT excites SAWs by converting RF signals at the IDT's resonant frequency while the right IDT senses the mechanical wave and converts it back to the electrical domain. Such an IDT-to-IDT pair can 1) filter out RF signals which

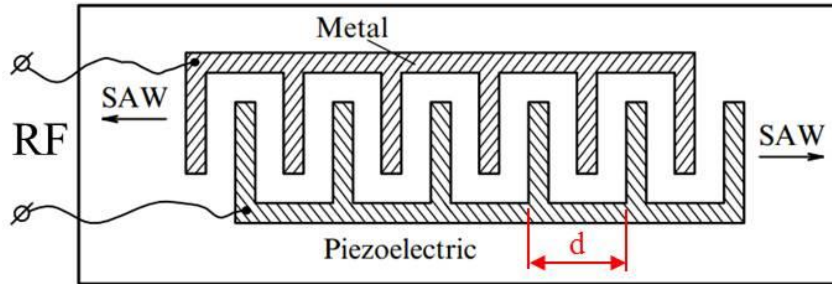

Figure 1-4: Top view of an interdigital transducer fabricated on a piezoelectric substrate for surface acoustic wave emission [2].

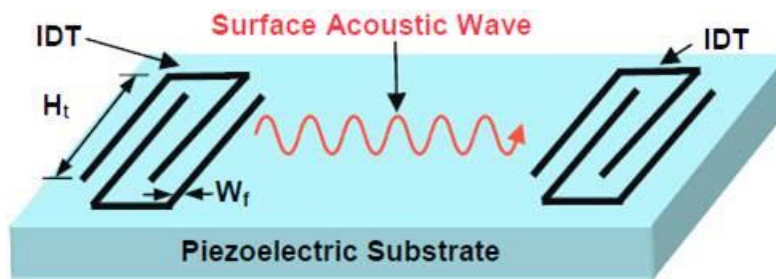

Figure 1-5: An IDT-to-IDT pair leads to numerous applications in various fields.

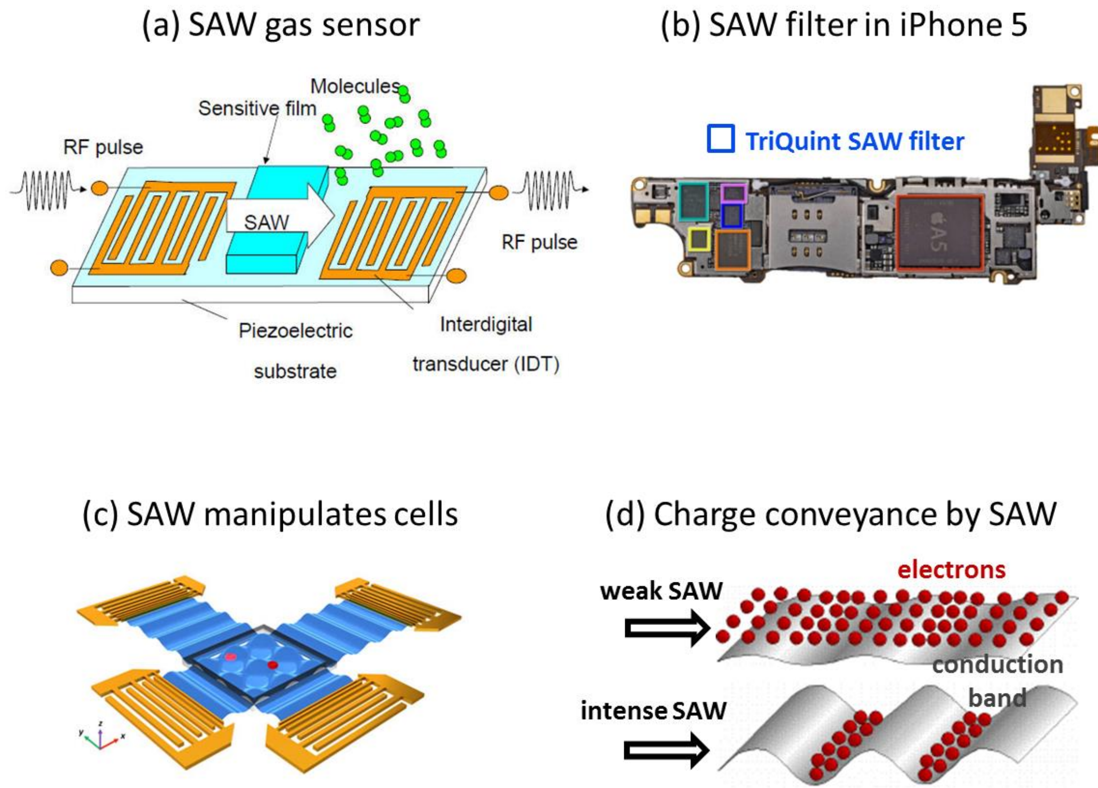

Figure 1-6: Various applications of surface acoustic waves (SAWs).

are not resonant with the IDTs, 2) form a delay line for which the delayed time is determined by the spacing between the two IDTs, or 3) be used to study the interaction between SAWs and the propagation surface by measuring acoustic power loss and velocity shift. Since the invention of IDT-to-IDT pairs, SAW devices have been extensively investigated and are currently widely used in many applications, including touchscreens [10], nondestructive ultrasonic diagnostics [11], chemical and gas sensors (see Figure 1-6a) [12], radio-frequency (RF) signal processors (see Figure 1-6b) [13], acoustoelectric devices [14, 15], microfluidic and micro-electromechanical actuators (see

Figure 1-6c) [16, 17], and devices utilizing dynamic quantum confinement (see Figure 1-6d) [18, 19].

1.2 Gallium Nitride Based Two-dimensional Electron Gas

A semiconductor which has received a great deal of attention recently is gallium nitride (GaN), which, interestingly, has a large piezoelectric effect [20] due to the polar nature of its hexagonal crystal structure (see Figure 1-8). AlGaN/GaN heterojunction-based high electron mobility transistors (HEMTs) [21, 22] have been considered for numerous emerging high-frequency high-power RF and microwave applications. For example, one important application under current investigation is to use small GaN HEMT chips to replace bulky transformers, in order to increase the conversion efficiency of electrical grids and improve their reliability by using wireless chips, and thus enhance the nation's energy security [23]. Furthermore, because of its wide band gap corresponding to relatively high photon energy, GaN is a critical enabler for blue and green light sources that do not require optical frequency doubling. Recently, green InGaN/GaN light emitting diodes (LEDs) [24] and laser diodes [25] have been demonstrated.

HEMTs are based on a heterojunction usually consisting of 20 nm $Al_{0.25}Ga_{0.75}N$ and 1 μm GaN, as shown in Figure 1-9. Due to the strong piezoelectric field caused by the highly strained AlGaN layer (which has a smaller lattice constant than the GaN under-layer as shown in Figure 1-10 [26]), a sheet of charge known as a two-dimensional electron gas (2DEG) is formed at the AlGaN/GaN interface, creating a channel between the source and drain electrodes. When the gate-source voltage is above a threshold value,

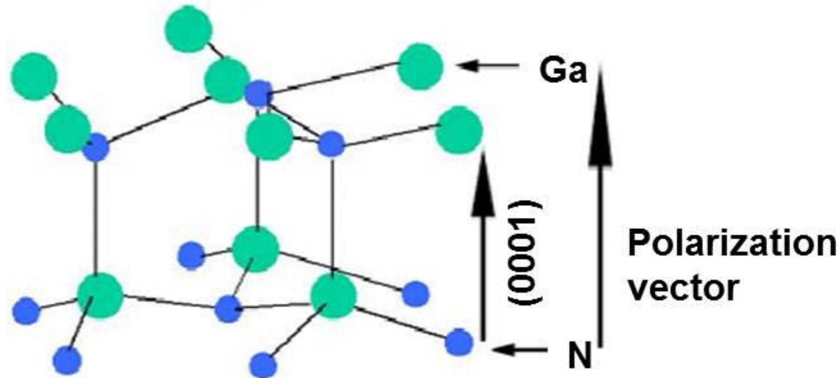

Figure 1-7: Crystal structure of GaN and the built-in polarization vector.

the channel is filled with a great number of electrons and is highly conductive. With the HEMT in this “on” state, voltage applied across the source and drain electrodes causes electron drift and hence electrical current between the source and the drain. On the other hand, when the gate-source voltage is below a certain threshold value, the channel becomes depleted of electrons and is highly resistive. In this case, the HEMT is in the “off” state and an applied source-drain voltage yields only a small electrical current.

The mechanical strain at the interface is strongly linked by piezoelectric coupling to the 2DEG carrier density and hence can be dynamically modulated by varying the gate-source voltage, which controls the 2DEG carrier density. We will show in later chapters that this dynamic relaxation of the built-in strain in the AlGaN layer yields SAWs, and hence a GaN HEMT can be operated as an acoustic wave emitter.

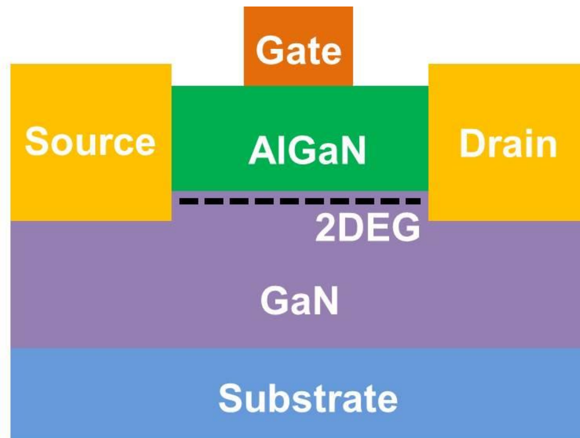

Figure 1-8: A conventional AlGaN/GaN high electron mobility transistor structure. The dotted line indicates the 2DEG channel that connects the source and drain.

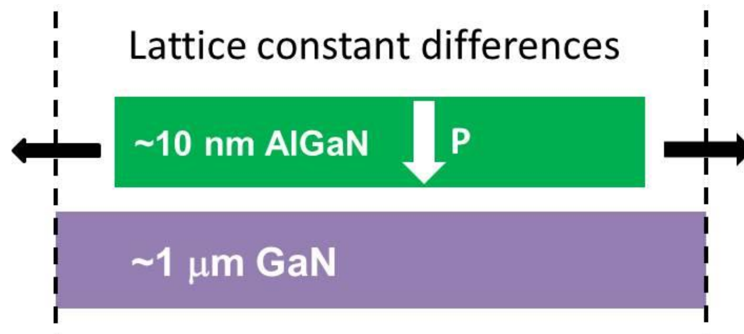

Figure 1-9: Built-in tensile strain in AlGaN layer due to lattice mismatch.

1.3 Active Acoustic Emitter Based on a 2DEG

Traditional acoustic wave devices such as FBARs and IDTs are passive and offer little DC voltage control over characteristics of the emitted acoustic waves (e.g., intensity, resonant frequency, and emission pattern) once the devices are fabricated. Interestingly, acoustic wave emitters based on active devices such as transistors allow interactions between the emitted acoustic waves and the transported charge carriers, leading to schemes for active control of acoustic emission.

The GaN HEMT is an active device that can emit SAWs by RF modulation of the carrier density in a 2DEG channel, as suggested in Section 1.2. Because of the various regimes of charge transport in a 2DEG corresponding to ranges of applied DC bias, GaN HEMTs could provide certain means to actively control the characteristics of the emitted acoustic waves. First, because the same RF voltage modulation leads to different 2DEG carrier density modulations at different HEMT DC bias points, the 2DEG provides a means for DC voltage tunable intensity of SAW emission. Second, carrier drift in a certain direction (source-to-drain or drain-to-source) can amplify or attenuate SAW modes propagating in that direction (depending on the electron velocity relative to the SAW velocity) [2] and therefore can enable controlled directional intensity of SAW emission. Finally, the 2DEG offers the potential for switchable SAW emission, i.e., the ability to transduce different SAW modes at different HEMT DC bias points.

GaN-based epitaxial structures are usually grown on substrates such as sapphire, silicon, or silicon carbide due to difficulty obtaining bulk GaN substrates. SAW modes which are supported by GaN-on-sapphire are Rayleigh (R), Love (L), Sezawa (S) and

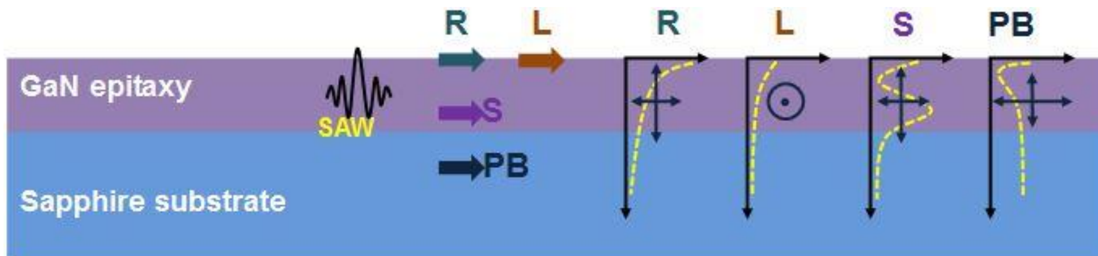

Abbr.	Full name	Penetration depth	Polarization
R	Rayleigh	surface of epitaxy	in-plane, primarily vertical
L	Love	surface of epitaxy	out-of-plane
S	Sezawa	deep epitaxy	in-plane, primarily vertical
PB	pseudo-bulk	epitaxy / substrate	in-plane, primarily horizontal

Figure 1-10: SAW modes supported by a GaN-on-sapphire structure.

pseudo-bulk (PB) modes, which propagate with different polarizations and at different depths within the epitaxial layer structure as shown in Figure 1-11 [27]. The Rayleigh and Love modes are primarily confined on the surface of the thin film epitaxy. The existence of the Love mode, which is usually piezoelectrically inactive in hexagonal wurzite nitrides, is due to polarization mixture caused by the trigonal/3m sapphire substrate that supports SH and leaky SH modes [27]. The Sezawa (SV polarized) modes are higher-order R modes propagating deep in the epitaxial layer and can only be excited if the epitaxy thickness is comparable to the acoustic wavelength. The PB modes (SV polarized, primarily longitudinally) extend deep into the sapphire substrate [28]. Different types of acoustic waves can have advantages for different applications. For example, Rayleigh waves are the easiest to excite and most commonly used, but suffer huge losses at solid-liquid interfaces; at such interfaces, Love waves are usually used because of relatively small damping of shear horizontal modes by liquids.

In addition to the potential for active control over emitted SAWs, 2DEGs can also have significantly stronger coupling to SAWs than IDTs can. Recent SAW applications such as microfluidic actuators [16, 17] and dynamic quantum confinement devices [18, 19] require intense acoustic beams; traditional interdigital transducer (IDT) methods need 50 or more pairs of fingers to reach sufficient intensities and therefore occupy relatively large real estate on a chip (hundreds of micrometers to several millimeters in length) compared to a HEMT (~10 micrometers in length) of similar width. The vertical (cross-plane) strain modulation induced by electrical modulation of one pair of conventional IDT electrodes is given by:

$$\Delta\gamma_{zz} = \sum_i d_{3i} \Delta E_i \tag{1.1}$$

where d_{3i} are the piezoelectric strain coupling constants in the vertical direction and ΔE_i are the modulated components of applied electric field in the $i = x$, y, and z directions. For a typical IDT geometry (1 μm wide electrodes with 4 μm periodicity) and voltage modulation (1 V peak-to-peak) on a lightly-doped GaN substrate, finite element simulation of the resulting field profile indicates $\Delta E_z \approx 0.5$ MV/m in the vertical (cross-plane) direction and $\Delta E_x \approx 1$ MV/m in the horizontal (in-plane) direction. For c-plane GaN ($d_{31} = 0$, $d_{32} = 0$, and $d_{33} = 2.19\times10^{-12}$ C/N [20]), finite element simulation and Equation 1.1 each indicate modulated vertical strains on the order of 10^{-7} to 10^{-6}. Other common SAW substrates (e.g., GaAs, $LiNbO_3$, $LiTaO_3$, and ZnO) also yield modulated strains on this order, with the exception of PZT, which can achieve strains on the order of 10^{-4}. However, PZT has drawbacks for monolithic integration with devices made from GaN and other III-V semiconductors [29, 30].

Equation 1.1 can also be used to estimate the modulation in 2DEG vertical (cross-plane) strain due to a change in carrier density $\Delta n^{(2)}$ by solving for ΔE_i using Poisson's equation with the boundary conditions of an AlGaN/GaN heterostructure, yielding [31]:

$$\Delta\gamma_{ZZ} = \frac{e_{33}e_0\Delta n^{(2)}}{\varepsilon\varepsilon_0 C_{33} + e_{33}^2} \tag{1.2}$$

where e_{33} is the piezoelectric stress constant that couples electric field and stress in the vertical direction, e_0 is the electron charge, ε is the relative permittivity, ε_0 is the vacuum permittivity, and C_{33} is the elastic stiffness constant in the direction corresponding to e_{33}. For a c-plane $Al_xGa_{1-x}N$/GaN-based 2DEG, $e_{33} = 0.65+0.9x$ C/m^2, $\varepsilon = 5.35-0.58x$, and $C_{33} = 398-9x$ GPa [31], yielding $\Delta\gamma_{zz}$ on the order of 10^{-4} for $x = 0.25$ and a change in carrier

density $\Delta n^{(2)} \approx 10^{13}$ cm^{-2}, which is typical for 2DEG modulation in this material system [22]. This calculation suggests that a 2DEG in GaN is able to generate strain modulation between two and three orders of magnitude greater than that achieved by a single IDT pair on the same substrate at the same applied RF voltage.

In this work, we explore the coupling between an electrically pumped 2DEG and acoustic waves. In Chapter 2, we verify the emission of SAWs from a 2DEG by experimentally examining AlGaN/GaN HEMTs and monolithically integrated IDTs which function as acoustic wave detectors. We also demonstrate detection of incident SAWs by a 2DEG due to piezoelectric coupling. In Chapter 3, we characterize the frequency spectrum of SAWs emitted by a 2DEG and study the principle of switchable SAW emission by a 2DEG. In Chapter 4, we perform modeling to understand SAW amplification or attenuation by electron drift current in a 2DEG and investigate directional SAW emission from a 2DEG under certain bias conditions.

Chapter 2

Emission and Detection of SAWs by a 2DEG

In this chapter, we use integrated IDTs as SAW sensors to the demonstrate emission of SAWs by AlGaN/GaN HEMTs under certain bias conditions through dynamic screening of the HEMT's vertical field by modulation of its 2DEG. We show that a strong SAW signal can be detected if the IDT geometry replicates the HEMT electrode geometry at which RF bias is applied. In addition to characterizing SAW emission during both gate-source and drain-source modulation, we demonstrate SAW detection by HEMTs.

2.1 Previous Work

GaN-based materials are known to exhibit large acoustic velocities, low acoustic attenuation, and strong piezoelectric effects [32], leading to their use in gigahertz (GHz) band SAW devices [33-35]. For example, studies have shown that the attenuation of SAWs propagating in a AlGaN/GaN heterostructure can be controlled by a DC-biased

diode that depletes the 2DEG between the IDTs emitter/receiver pair [36]. While monolithically integrated HEMTs have previously been used to amplify the electronic signal measured by an IDT [37], and one study examined how HEMT characteristics are affected by flexural modes when the HEMT is grown on an electromechanical resonator [38], no studies have examined the direct interaction of SAWs and HEMTs, i.e., the generation or detection of SAWs by a 2DEG that is dynamically modulated in the various regimes of transistor operation (e.g., cutoff, linear, and saturation regions) possible for a 3-terminal HEMT.

Several interesting applications would be enabled should HEMT bias conditions exist in which significant energy is coupled directly from HEMT electronic modulation to SAW modes or vice-versa. In high-power and high-speed RF and microwave applications of HEMTs, material degradation due to thermal [39] and acoustic [40, 41] stresses can pose a significant problem, prompting studies of device reliability [42]. SAWs emitted by a HEMT could provide a means to nondestructively sample the degradation of its epitaxy and 2DEG in real time, since SAW attenuation is known to depend strongly on crystal quality [11].

Furthermore, SAWs incident on a HEMT could potentially provide dynamic strain modulation of the HEMT [38] (and thereby modulate its 2DEG carrier concentration and carrier mobility) over short times, potentially without the degradation effects that often occur when such strain is incorporated through lattice mismatch. Likewise, HEMT-based SAW detectors could provide a means for direct electrical amplification of SAW signals.

The potential for highly efficient HEMT-SAW coupling is supported by optical reflectance studies performed directly on an AlGaN/GaN HEMT, which showed strong generation of coherent acoustic phonons near the drain due to dynamic screening by the HEMT's 2DEG [43]. Here we use integrated IDTs to confirm both the generation and detection of SAWs by AlGaN/GaN HEMTs and study the dependence of these mechanisms on HEMT frequency and DC bias conditions.

2.2 Device Design and Fabrication

The monolithically integrated HEMT-IDT structure used for this chapter is shown in Figure 2-1. The expitaxial structure is based on an undoped heterojunction consisting of 20 nm AlN nucleation, 1.5 μm GaN, 20 nm $Al_{0.25}Ga_{0.75}N$, and a 2 nm GaN cap grown by molecular beam epitaxy on a sapphire (0001) substrate (see Figure 2-2). The AlGaN/GaN lattice mismatch strain creates a built-in piezoelectric polarization field at the heterointerface, which causes a 2DEG to accumulate.

Figure 2-3 shows the fabrication process of the integrated HEMT-IDT structure. HEMTs were fabricated by chlorine etching mesas and e-beam evaporating Ti/Al/Ti/Au Ohmic contacts (subsequently exposed to rapid thermal annealing) and Ni/Au Schottky gates. The processed HEMTs had 1-μm-wide gates equidistant between 7-μm-wide source and drain contacts that had a 7 μm separation (see Figure 2-2). Ni/Au IDTs were formed during gate deposition.

Three different IDT designs were fabricated and used for different purposes as shown in Figure 2-4; one IDT geometry had an electrode periodicity of 14 μm with the

same widths and spacing as the HEMT source and gate (see Figure 2-4a), a second had an electrode periodicity of 28 μm with the same widths and spacings as the HEMT source

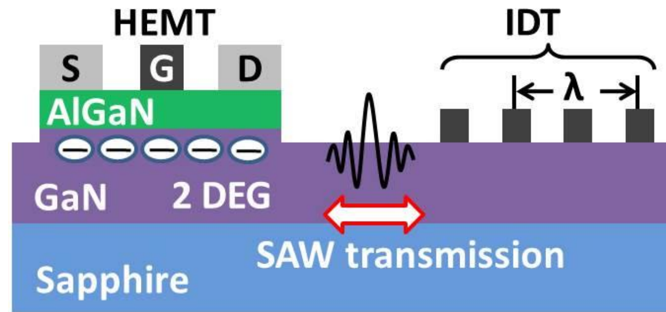

Figure 2-1: Integrated HEMT-IDT structure.

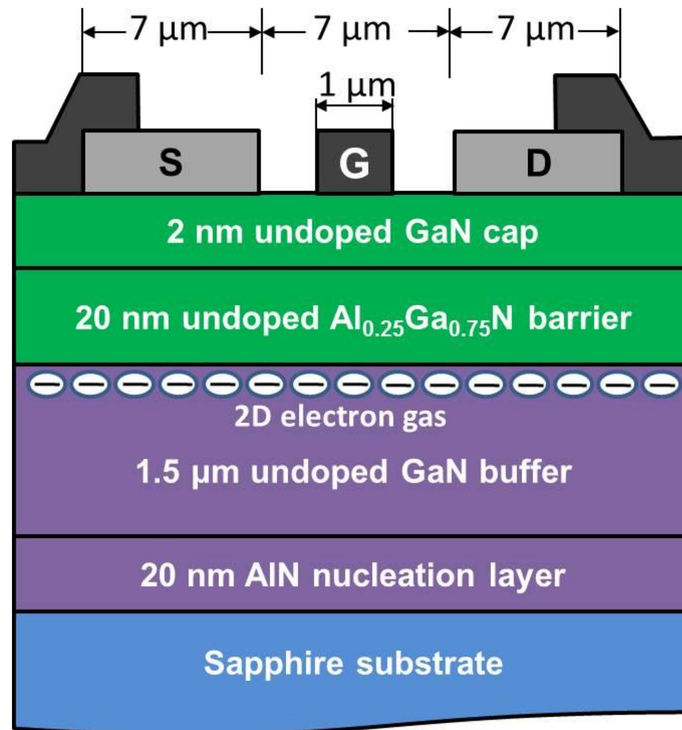

Figure 2-2: Design of the epitaxial layer structure.

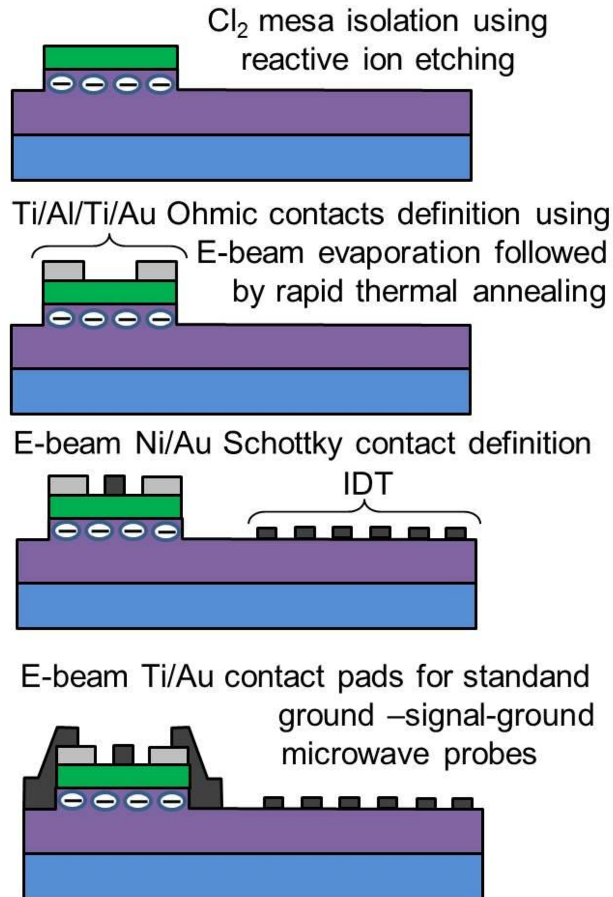

Figure 2-3: Micro-fabrication process of the integrated HEMT-IDT structure.

and drain (see Figure 2-4b), and a third had a larger electrode geometry with periodicity 40 µm that was not resonant with the HEMT geometry (see Figure 2-4c).

IDT-IDT pairs were also fabricated for each of these geometries to characterize the SAW properties of the epitaxial layers; transmission characteristics were measured for both as-grown (unetched) AlGaN/GaN/sapphire heterostructures (corresponding to the HEMT layers in which SAWs were generated) and etched GaN/sapphire heterostructures (corresponding to the region outside of the HEMT through which SAWs

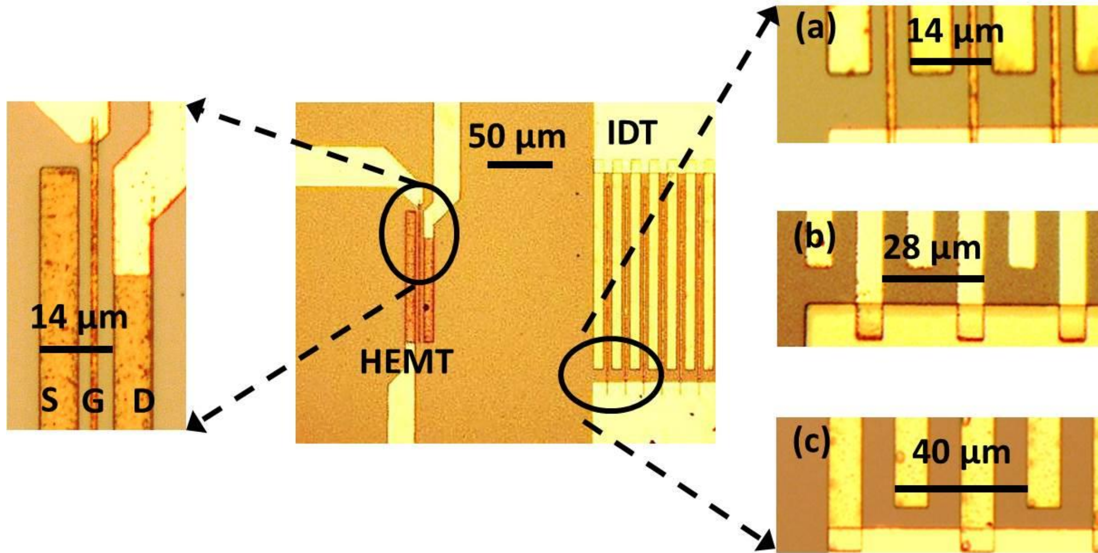

Figure 2-4: Optical images of the fabricated HEMT-IDT structure and three different designs of IDTs, indicated as (a), (b) and (c).

propagated). The distances between HEMTs and IDTs and between IDT pairs were nearly the same (approximately 120 μm).

2.3 Acoustic Emission from a 2DEG

Acoustic emitters (either HEMTs or IDTs) were contacted by standard microwave probes (GGB 40A-GSG-100-DP) and operated by a network analyzer (Agilent 8753C), a DC power supply (Agilent E3631A), and a bias tee which combined RF and DC signals. The network analyzer operated the device by sweeping the applied RF frequency from 100 MHz to 1 GHz and also receiving the RF signal from an IDT detector. The detected RF power divided by the applied RF power throughout the swept frequency is calculated (see Figure 2-5).

Figure 2-6a demonstrates the IDT-to-IDT transmission characteristics of the unetched heterostructure for the 14 μm IDT geometry displayed in Figure 2-4a, showing SAW peaks at 307.7 and 713.2 MHz corresponding respectively to the Rayleigh (R) and pseudo-bulk (PB) modes [27] of the epitaxial layer structure. IDT-IDT transmission characteristics of the etched heterostructure showed significantly lower insertion loss due to the removal of the 2DEG and consequent reduced attenuation [44]; however, the etching process introduces surface roughness which is expected to contribute to SAW scattering. Impedance mismatch in IDT-IDT and HEMT-IDT structures as well as mass loading by the thick electrodes [44] (IDT fingers and HEMT gates were deposited simultaneously; the latter requires a thick layer to reduce electrical impedance) also contribute to insertion loss for HEMT-IDT structures and both etched and unetched IDT-IDT pairs.

2.3.1 Source-Gate Modulation

When the drain-source voltage (V_{DS}) of the HEMT was held at 10 V and the gate-source voltage (V_{GS}) was driven with a 1.8 V peak-to-peak ($V_{p\text{-}p}$) RF signal about zero volts (i.e., the DC bias point shown in Figure 2-7), a 307.7 MHz peak was detected at the IDT in the gate-source geometry as shown in Figure 2-6b. This peak frequency was the same as that of the Rayleigh mode in the IDT-to-IDT geometry, confirming the emission of SAWs by the modulated HEMT. The larger insertion loss of the HEMT-IDT structures compared to that of the etched IDT-IDT structures is likely primarily due to the much smaller number of “fingers” in the HEMT (1 pair) than in the transmitter IDT (30 pairs).

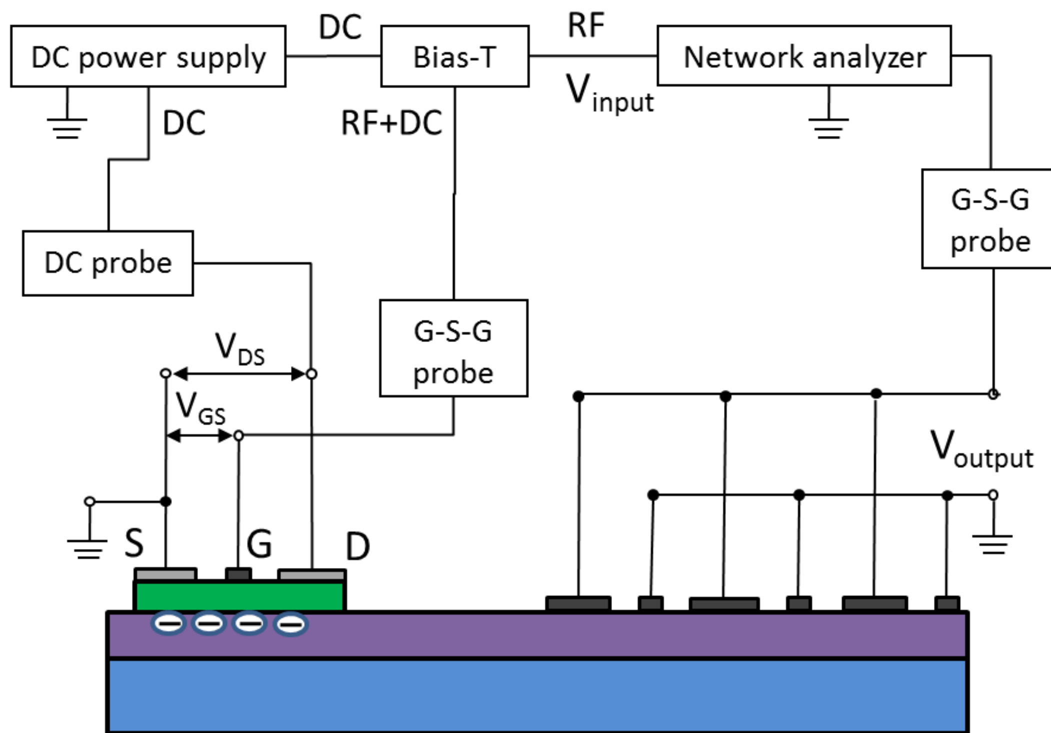

Figure 2-5: Setup for characterization of the HEMT-IDT transmission while the RF signal is applied to the V_{GS}.

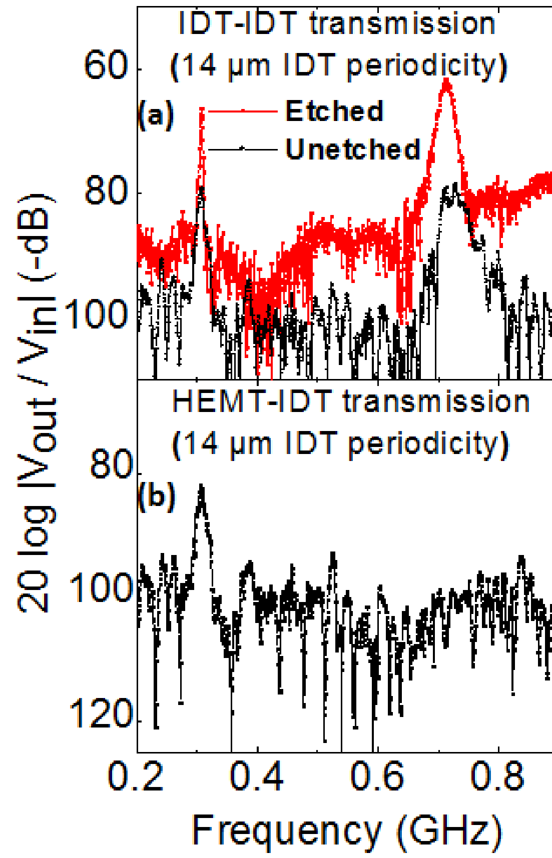

Figure 2-6: IDT-IDT transmission and HEMT-IDT transmission when the RF signal is applied across and source-gate electrodes.

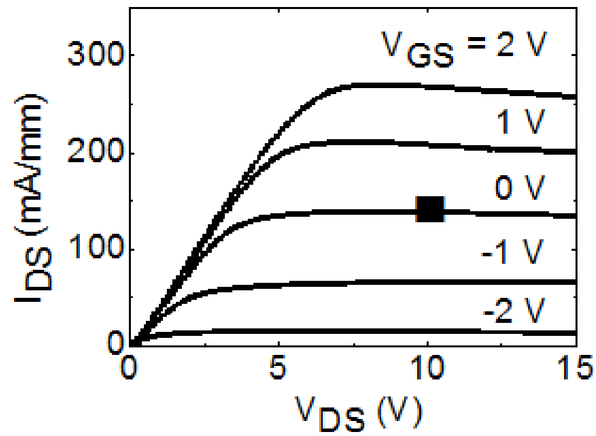

Figure 2-7: HEMT DC characteristics and bias point in Figure 2-6b.

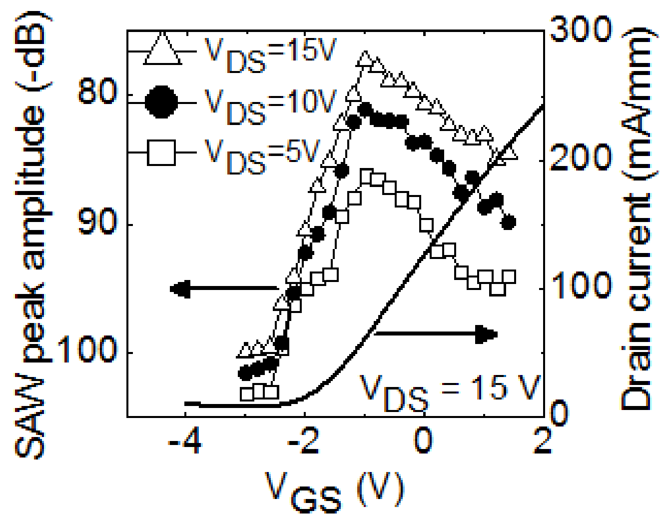

Figure 2-8: Amplitude of SAW peak as a function of VDS and the DC component of V_{GS}.

To study the dependence of the 307.7 MHz SAW peak on HEMT bias conditions, its amplitude is plotted versus $V_{GS,DC}$ for several V_{DS} values in Figure 2-8. The drain current (I_{DS}) as a function of $V_{GS,DC}$ is also shown, indicating a HEMT threshold voltage (V_{th}) at $V_{GS,DC}$ = -2 V. Because the horizontal electric field in the HEMT does not produce strain to the first order [45], we expect modulation of the vertical electric field (E_Z) across the AlGaN/GaN layers to play the primary role in SAW generation. For all values of V_{DS}, the maximum HEMT-to-IDT SAW transmission occurs when $V_{GS,DC} \approx V_{th} + V_{P-P}/2 = -1.1$ V; at this bias point, there is maximum time variation of the carrier density in the 2DEG, to which we ascribe increased SAW generation through screening of E_Z [43]. Such screening has been predicted through self-consistent Schrödinger-Poisson calculations to be quite significant [31] and has been identified as a mechanism by which stress-induced defects are produced in the AlGaN barrier layer and device degradation occurs [40].

In addition, the fact that the pseudo-bulk mode at 713.5 MHz was not observed is further evidence that SAW generation takes place close to the surface (i.e., near the 2DEG) when gate-source modulation (which oscillates the 2DEG carrier density) is applied. Furthermore, Figure 2-6b shows that the amplitude of the emitted SAW peak increases with higher V_{DS}. We attribute this to increasing depletion of carriers in the GaN layer between the gate and drain, leading to greater penetration of the dynamically screened vertical field into the GaN layer and larger spatially-averaged vertical field magnitude in this region [41, 46, 47].

2.3.2 Source-Drain Modulation

The fabricated HEMTs were also operated in common-gate mode with V_{GS} held constant and V_{DS} driven with a 1.8 V_{P-P} RF signal about a DC bias point. As illustrated in Figure 2-9b for V_{GS} = 3V and V_{DS} = 1 + 1.8V_{P-P}, the 28 μm (Figure 2-4b) IDT geometry in this case detected SAW peaks emitted by the HEMT at 195.1 and 368.4 MHz, consistent with Rayleigh and pseudo-bulk modes (note that these are lower in frequency than the Rayleigh and pseudo-bulk modes discussed above due to the larger electrode periodicity). The fact that both peaks were detected is consistent with the HEMT source and drain acting as conventional IDT fingers when modulation is applied to them, with dynamic strain extending into the substrate.

As shown in Figures 2-9c and 2-9d, the magnitudes of these modes are controlled by V_{GS} and maximized for small DC values of V_{DS} and high values of V_{GS}. When V_{GS} is below threshold, the 2DEG is depleted, and the vertical field profile does not change significantly as V_{DS} is varied [47]; hence modulation of V_{DS} for low V_{GS} does not lead to significant SAW generation. Above threshold, for small DC values of V_{DS}, dE_Z/dV_{DS} is large (due to carrier depletion effects as discussed above [41]), leading to significant SAW generation as V_{DS} is modulated. As the DC value of V_{DS} increases, dE_Z/dV_{DS} saturates [47], leading to reduced SAW generation.

In addition to this effect, it is well known that SAW generation is not as strong when Ohmic contact fingers are formed on a conductive substrate [34], which is the case for the HEMT's source and drain electrodes. This was confirmed by separate measurements we made using IDT-IDT pairs in which all fingers were Ohmic, which

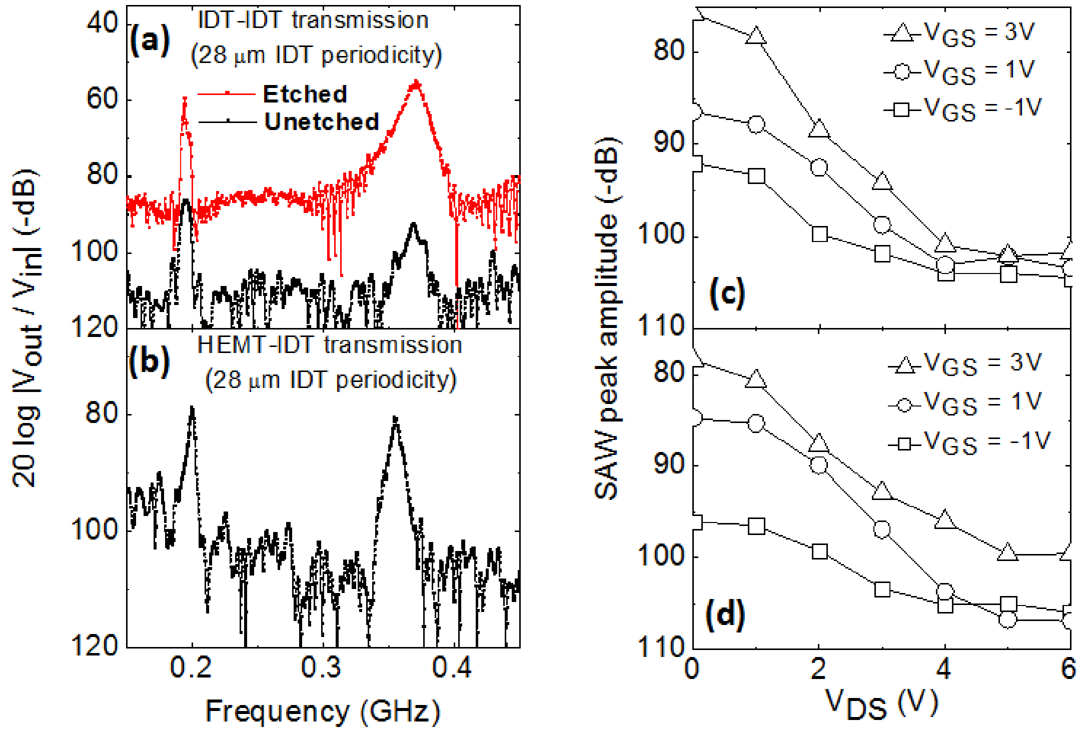

Figure 2-9: Characterization of the HEMT-IDT transmission while the RF signal is applied across the source-drain electrodes.

showed that SAW generation became weaker as the DC bias point about which the RF signal was added increased.

2.4 Acoustic Detection by a 2DEG

Finally, we studied the detection of SAWs by AlGaN/GaN HEMTs. In this case, an IDT with a periodicity of 40 μm (Figure 2-4c) was used to transmit SAWs to a HEMT with both V_{GS} and V_{DS} held at a constant DC bias point. A schematic diagram of such an IDT-to-HEMT transmission is illustrated in Figure 2-10. IDT-to-IDT transmission characteristics for the 40 μm IDT geometry are shown in Figure 2-11a.

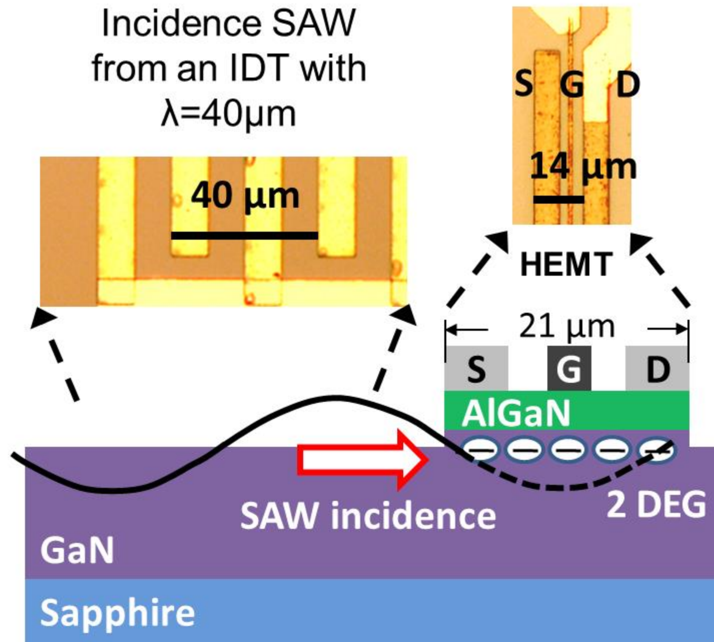

Figure 2-10: Detection of incident SAWs by a 2DEG.

The AC admittance ($I_{DS,AC}/V_{IDT,AC}$) was used to quantify detection of the SAW by the HEMT, and is plotted in Figure 2-11b for the DC bias point shown in the inset. The Rayleigh mode is clearly visible in the AC admittance spectrum, demonstrating that the HEMT can sensitively detect piezoelectric modulation of the 2DEG that occurs when a Rayleigh mode (confined at the surface) passes through it.

As shown in Figure 2-12, the AC admittance amplitude is controlled by V_{GS} and roughly follows the HEMT DC characteristics. When the HEMT is biased in its linear regime, the 2DEG density is relatively uniform from the source to the drain, so the small carrier density variation caused by the strain modulation has negligible effect. When the

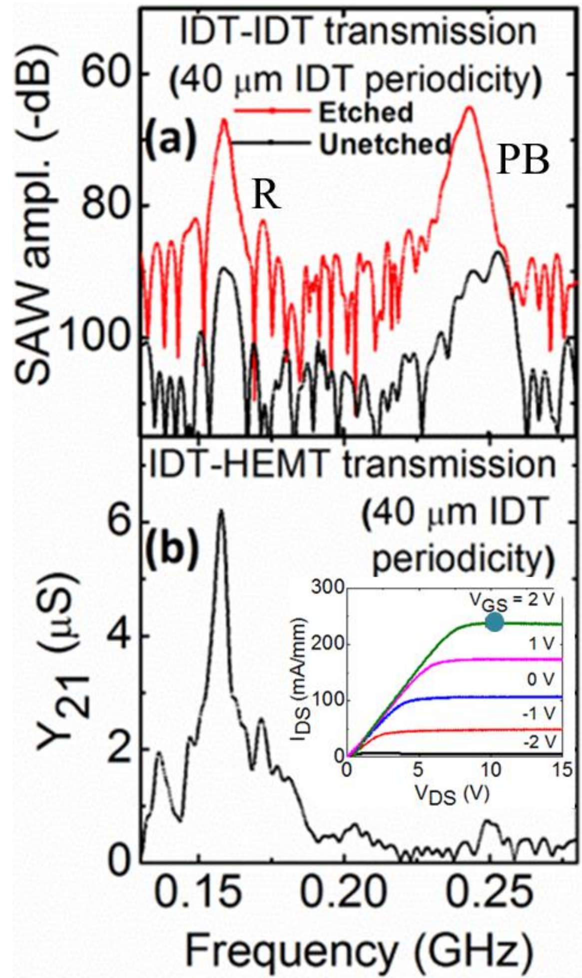

Figure 2-11: IDT-IDT transmission and IDT-HEMT transmission in which the HEMT is operated at the DC bias point shown in the inset.

HEMT enters its saturation regime, however, pinch-off of the 2DEG occurs on the drain side; even a small variation of the carrier density in the pinch-off region caused by the strain wave has a significant effect on the HEMT's electrical characteristics, causing the AC admittance to rise rapidly. This change in admittance can be greatly increased by impedance-matching the RF source and IDT, which is expected to increase the magnitude of the generated SAW mode by as much as a factor of 1000 [34].

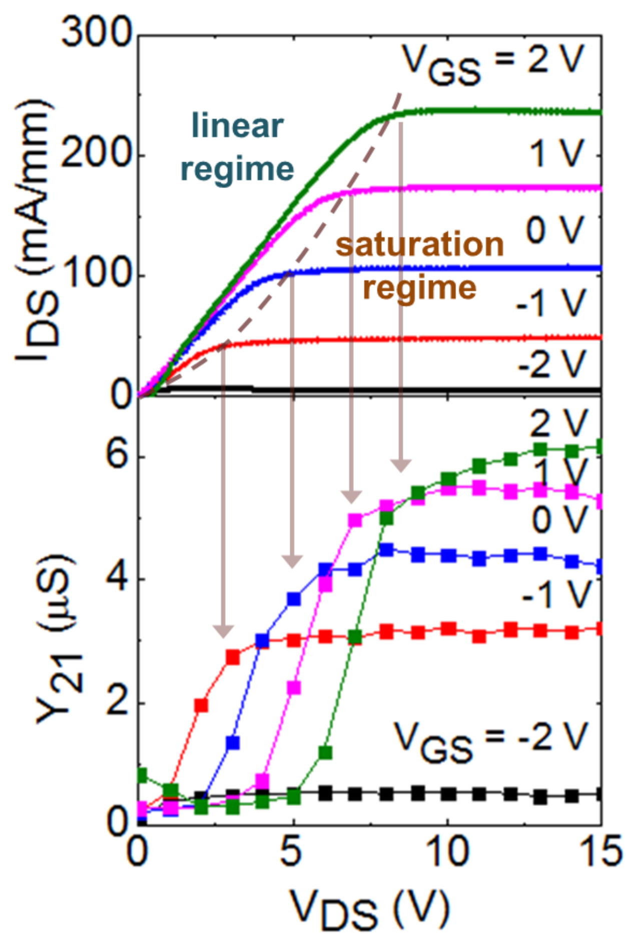

Figure 2-12: AC admittance under various HEMT operation conditions.

2.5 Conclusion

In conclusion, we have used integrated IDTs to confirm the generation of SAWs by AlGaN/GaN HEMTs, and have shown how different bias and frequency conditions can be used to reliably transduce Rayleigh and pseudo-bulk modes.

The relatively high signal-to-noise ratio observed in measuring these modes suggests that a HEMT could be occasionally driven with appropriate bias conditions to emit SAW pulses that would nondestructively sample material degradation of the 2DEG (for Rayleigh modes) or GAN/substrate interface (for pseudo-bulk modes) in real time. Such an integrated HEMT-IDT system can also potentially improve device reliability and reduce cross-talk by damping the strong vibrational modes that propagate across the chip, and possibly provide a means to efficiently manage device heating by resonantly removing energy from vibrational modes with high effective temperature. Furthermore, we demonstrated the detection of SAWs by a HEMT, which may enable high-speed, amplified detection of SAWs for sensing applications [38] or dynamic strain modulation of a HEMT's electrical properties.

Because an IDT can only detect SAWs which are resonant with its geometry, HEMT-IDT transmission cannot provide the full spectrum of SAWs emitted from a HEMT. In order to characterize the full spectrum, the next chapter will present an optical reflectance method that can measure the various SAW modes supported by a GaN-on-sapphire structure and the active control of these modes by HEMT DC bias.

Chapter 3

Active Control of SAW Emission

In this chapter, optical reflectance spectroscopy is used to measure the full acoustic spectrum emitted by a modulated GaN-based 2DEG, including various SAW modes that propagate with different polarizations and penetration depths within the epitaxial layer structure. It is shown that 2DEGs can be actively controlled to selectively transduce certain acoustic wave modes based on DC bias conditions, because of their ability to provide either traditional bulk piezoelectric transduction or 2DEG transduction depending on whether the 2DEG is depleted or present.

3.1 Field Modulation in a HEMT

As discussed in Section 1.3, the primary SAW modes supported by a GaN-on-sapphire structure are Rayleigh (R), Love (L), Sezawa (S), and pseudo-bulk (PB) acoustic modes (Figure 1-11). Because our goal is to study the fundamental mechanisms of 2DEG acoustic emission rather than maximize conversion efficiency, we use a GaN layer thickness that is small (1.4 μm) relative to the acoustic wavelength (~20 μm), allowing us

to reduce the time, cost, and challenge of molecular beam epitaxy of the GaN layer and to have large device feature sizes, reducing the cost and processing complexity. It should be noted that this geometry prevents S modes from being efficiently transduced [33] and that significant room for optimization of the 2DEG emitter geometry remains.

It is important to distinguish the modulated electric field profiles and resulting acoustic modes emitted by a 2DEG layer structure in which the 2DEG is either depleted or present and which has the electrode geometry of either an IDT or HEMT (with DC bias applied across the drain/source and RF bias applied across the gate/source).

For the HEMT, if the 2DEG is depleted (e.g., by DC gate-source bias below threshold voltage), the field in the AlGaN layer is saturated by the drain-source voltage, and thus acoustic transduction by the modulated gate-source bias is minimal in this bias regime. Deeper into the structure, the field is not saturated, and RF modulation leads to PB emission. In the IDT structure with depleted 2DEG, field saturation occurs neither in the AlGaN layer nor deeper into the structure, and hence RF modulation leads to emission of all modes (R, L, and PB).

If the 2DEG is present, for the HEMT, the RF-modulated field is dropped mostly in the 2DEG channel, leading primarily to modulation of the vertical built-in piezoelectric field in the 2DEG and efficient coupling to the R mode (which is primarily vertically polarized) rather than PB modes (due to their quasi-longitudinal nature). In the IDT structure, the presence of the 2DEG attenuates the surface modes (R and L), making their emission weak, while the PB modes emitted are relatively strong since they are at a distance from the 2DEG and therefore less attenuated.

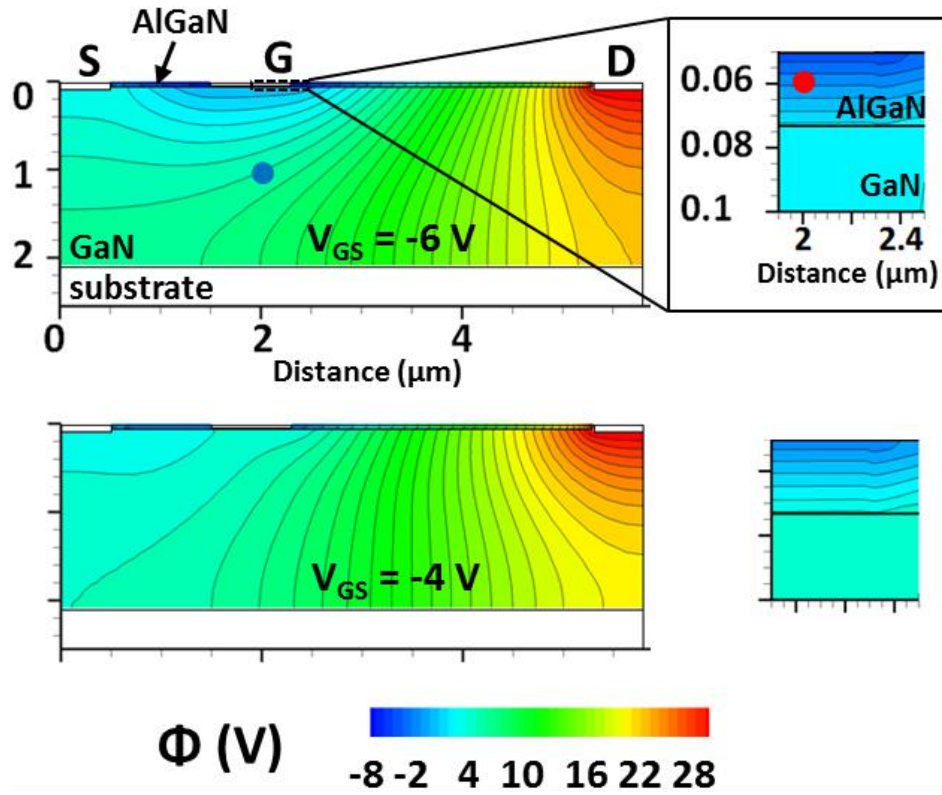

Figure 3-1: Potential distribution in a GaN/AlGaN heterostructure in which the 2DEG is depleted.

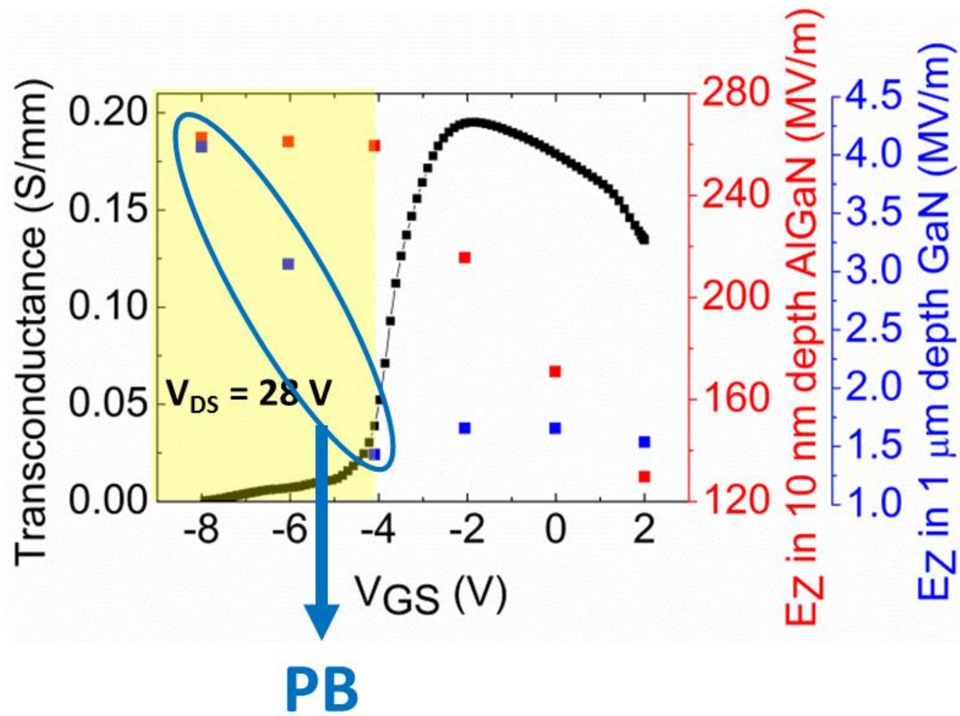

Figure 3-2: Transconductance of the simulated HEMT and DC-dependent electrical fields at two depths in the simulated epitaxy for the case in which the 2DEG is depleted.

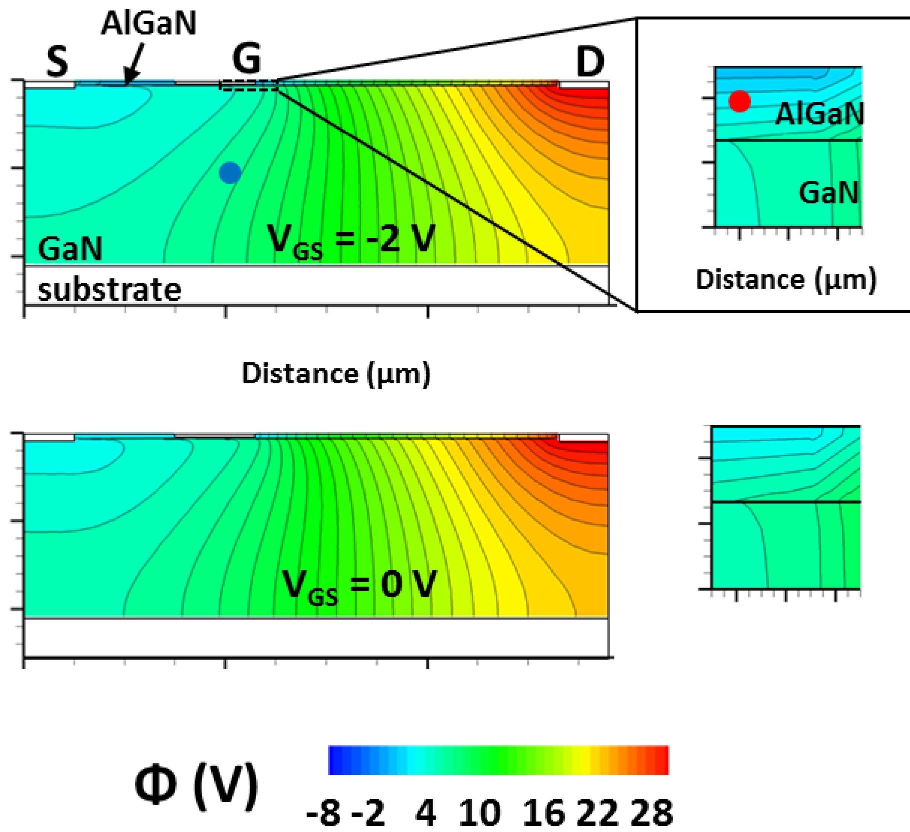

Figure 3-3: Potential distribution in a GaN/AlGaN heterostructure in which the 2DEG is present.

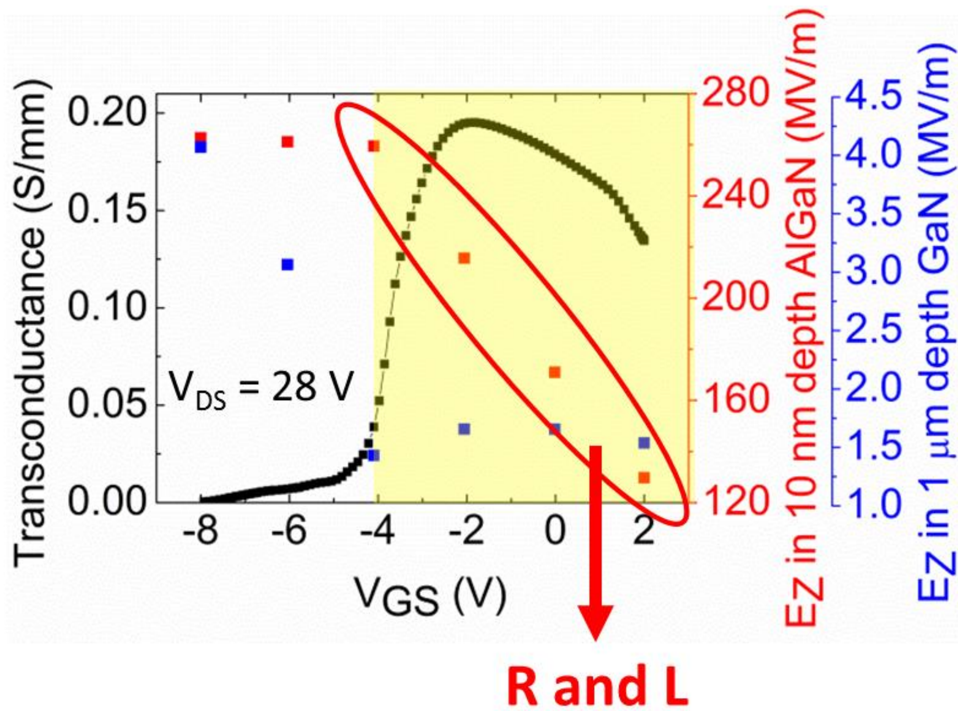

Figure 3-4: Transconductance of the simulated HEMT and DC-dependent electrical fields at two depths in the simulated epitaxy for the case in which the 2DEG is present.

2D finite-element simulations were performed to provide quantitative support of the above qualitative description of acoustic emission from a depleted or present 2DEG. A structure consisting of 20 nm $Al_{0.25}Ga_{0.75}N$ and 2 μm GaN was modeled using the Synopsys Sentaurus Device package [48]. The drain-source voltage (V_{DS}) was held at a constant 28 V and the gate-source voltage (V_{GS}) was varied from -6 V to 0 V with a step size of 2 V. The transconductance of the simulated HEMT is given in Figure 3-2 and shows a threshold of -4 V.

As the device is modulated between the two below-threshold points shown in Figure 3-1, the field modulation in the AlGaN layer is found to be small (since the total field is saturated in this region), while the modulation in the GaN is large. Above threshold (see Figure 3-3), the field modulation in the GaN is small since the modulated voltage drop occurs mostly in the 2DEG.

To compare the depth at which field modulation occurs (which influences the particular acoustic modes excited) at various bias points, two vertical electric field (E_Z) probes are shown as a function of V_{GS}: one in the AlGaN layer (10 nm depth) and the other in the GaN layer (1 μm depth). Figures 3-2 and 3-4 show that when the 2DEG is below threshold, modulation of V_{GS} leads to strong modulation of E_Z in the GaN layer but weak modulation in the AlGaN layer; this is reversed when the 2DEG is above threshold. PB modes are therefore expected to be preferentially emitted when the 2DEG is modulated below threshold, while surface modes (R and L) are expected to be emitted when the 2DEG is modulated above threshold.

3.2 Optical Reflectance Spectroscopy

To experimentally characterize acoustic emission from a 2DEG, we fabricated an undoped heterojunction epitaxial structure consisting of a 400 nm AlN layer, 1.4 μm GaN layer, 20 nm $Al_{0.25}Ga_{0.75}N$ layer, and 2 nm GaN cap layer on a sapphire (0001) substrate. Hall measurements at room temperature indicated a 2DEG carrier density and electron mobility of 1.6×10^{12} cm^{-2} and 800 cm^2/Vs. This mobility is low compared to most GaN-based 2DEGs, because of non-optimized epitaxy growth conditions.

HEMTs were fabricated by the same process described in Section 2.2. Ni/Au IDTs (50 pairs of fingers with a periodicity of 20 μm) were also fabricated on the as-grown (unetched) heterostructures. All HEMTs and IDTs were fabricated on the same chip and were aligned with the source/gate/drain electrodes and IDT fingers in the same direction. Fabricated devices and were RF-shielded and operated by a network analyzer, DC power supply, and bias tee.

The optical reflectance spectroscopy setup (see Figure 3-5) includes a continuous-wave (CW) HeNe laser (Thorlabs HNL225R), which was focused by a long working distance microscope objective (Mitutoyo M PLAN APO SL 50x) onto the sample with a spot size of 2 μm. The modulation of reflected intensity by an acoustic wave due to the photoelastic effect [49] was measured by an AC-coupled high-speed RF-shielded Si PIN photodetector (Menlo Systems FPD310-FV, frequency range 1-1500 MHz) and spectrum analyzer (Agilent N9340B), while the average power of the reflected light was monitored to confirm that it stayed constant. 2DEGs and IDTs were driven over the frequency range of 100 MHz to 1.1 GHz (with 1 V_{P-P} modulation applied to the gate/source electrodes for

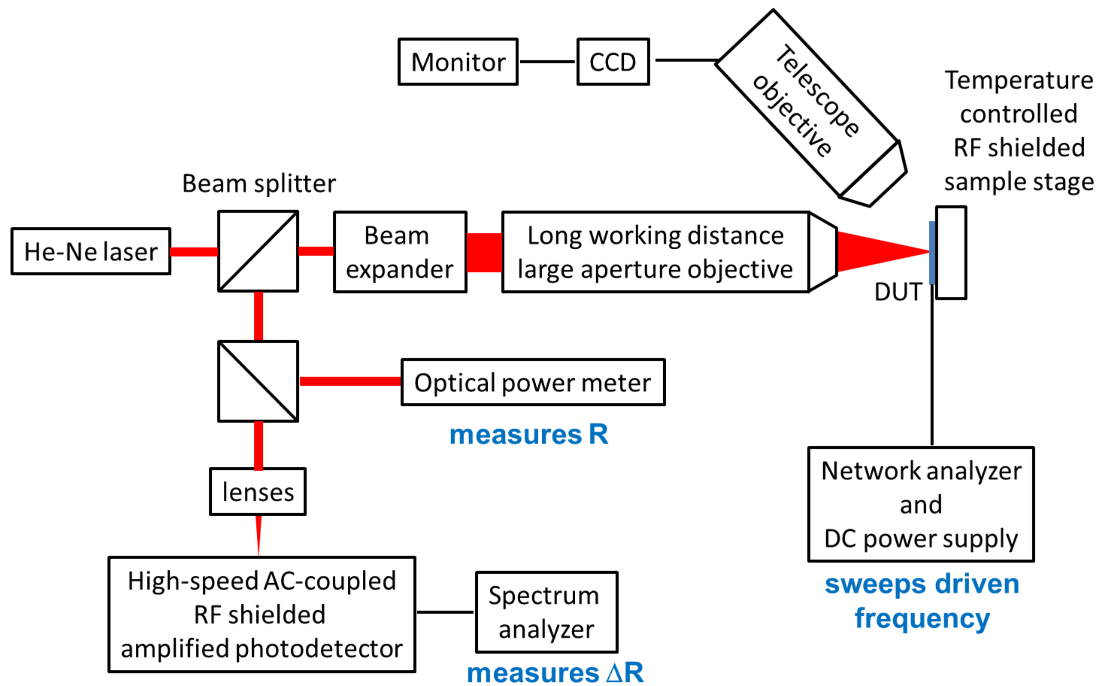

Figure 3-5: Optical reflectance spectroscopy setup used to measure ΔR/R (SAW amplitude) vs. bias frequency.

HEMTs and to consecutive finger pairs in IDTs); identical measurements were performed with the laser light blocked in order to confirm that measured spectra were not the result of RF leakage. Frequencies corresponding to multiples of the longitudinal mode spacing of the HeNe laser (257, 514, 771, and 1028 MHz) were skipped when sweeping the driving frequency.

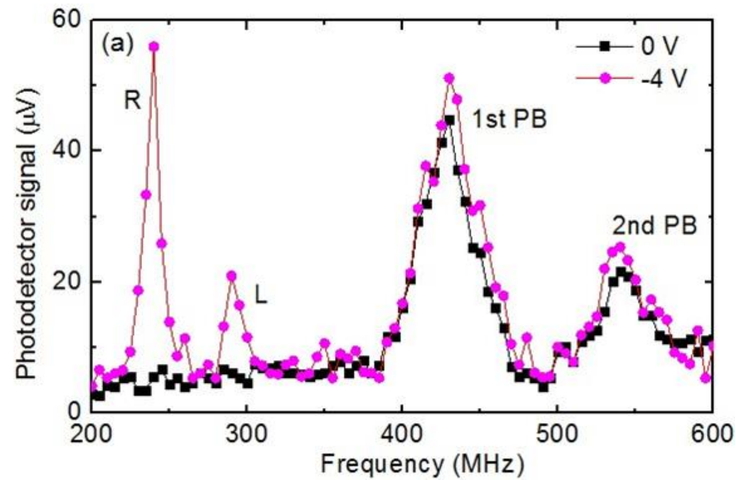

Figure 3-6: SAW spectrum emitted from an IDT under DC bias at 0V and -4V.

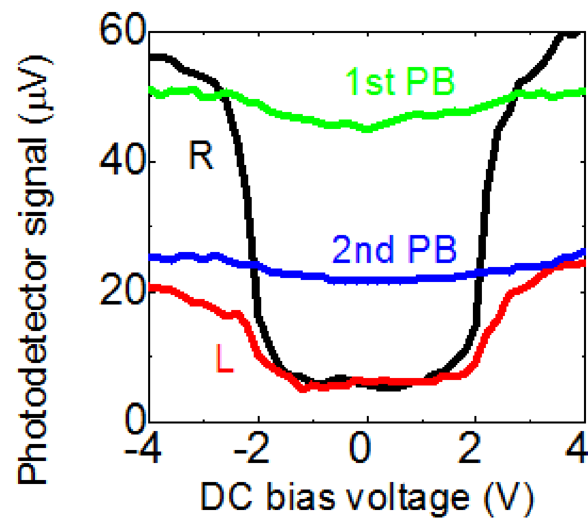

Figure 3-7: DC dependences of each resonant mode including R, L, PB1 and PB2.

3.3 SAW Mode Switching

3.3.1 Mode Dynamics in an Interdigital Transducer

The SAW spectrum emitted by an IDT and characterized by optical reflectance spectroscopy showed four prominent resonant modes (at 240, 290, 430, and 540 MHz) when a -4 V DC bias was applied, and only two modes (at 430 and 540 MHz) when the DC bias was zero, as shown in Figure 3-6. Based on the calculated dispersion relations for a GaN/sapphire layered structure [27], these modes at 240, 290, 430, and 540 MHz correspond to R, L, PB1, and PB2 modes respectively, and are consistent with a SAW wavelength of 20 μm.

As shown in Figure 3-7, the R and L modes are weakly emitted in the DC bias regime between -2 to 2 V (when the 2DEG is present), and strongly emitted in the DC bias regime > 2 V or < -2 V (when the 2DEG is depleted) [36]. However, the PB1 and PB2 modes are not affected by the DC bias, as predicted in Section 3.1.

3.3.2 Multi-gate HEMT

When a 4-gate HEMT was operated with its V_{DS} held at 10 V and its V_{GS} driven with an RF signal about 2 V, four resonant modes at 330 MHz (R), 420 MHz (L), 630 MHz (PB1), and 850 MHz (PB2) were observed by optical reflectance spectroscopy (laser spot located between the gate and drain electrodes) as shown in Figure 3-8a. These resonant frequencies are consistent with a periodicity of 14 μm. The amplitudes of all four SAW peaks are plotted versus $V_{GS,DC}$ (while V_{DS} is held at 10 V) in Figure 3-8b. When the device is modulated near its bias point of maximum transconductance, maximum time

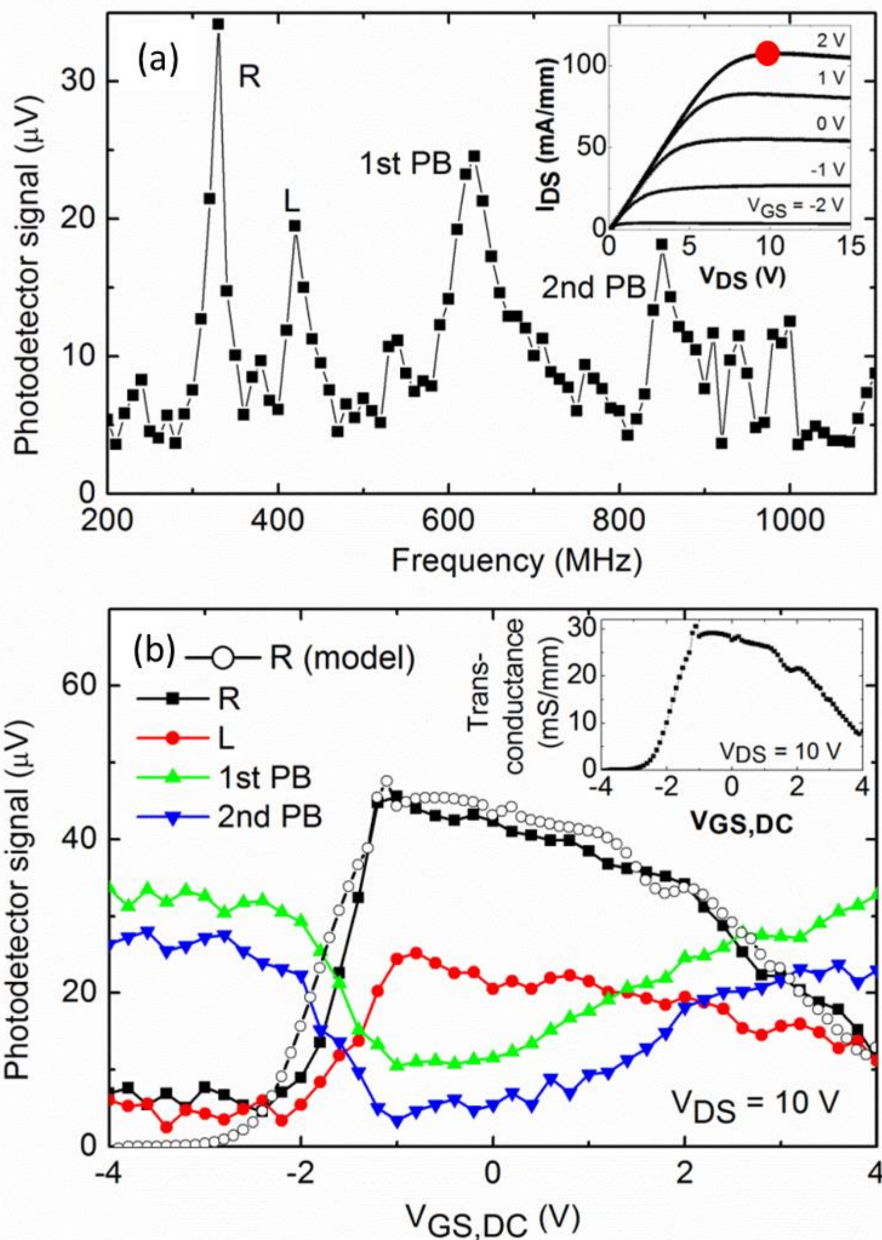

Figure 3-8: Characterization of the SAW emission spectrum of a 4-gate transistor and the DC dependences of the four primary acoustic modes (R, L, PB1 and PB2).

variation of the 2DEG carrier density occurs, and R and L modes are strongly emitted while PB1 and PB2 modes are weak. On the other hand, when the device DC bias is moved away from this point, the modulated voltage drop no longer primarily occurs in the 2DEG [50], and the PB1 and PB2 modes become strongly emitted while the R and L modes weaken. Different DC bias conditions therefore lead to SAW generation that is selective based on the modulation of the 2DEG carrier density or direct piezoelectric transduction by the dynamic potential. This selective source functionality in which R/L or PB modes can be chosen for emission based on the DC bias point is unique to the acoustic coupling provided by a 2DEG.

Based on the transconductance data shown in the inset of Figure 3-8b, the modulated carrier density as a function of the applied voltage (V_{GS}) can be derived using Equation 1.2 and used to predict the SAW signal detected by optical reflectance. Equation 1.2 can be rewritten as

$$\Delta\gamma_{ZZ} = \frac{e_{33} \cdot g_m}{\left(\varepsilon\varepsilon_0 C_{33} + e_{33}^2\right) \cdot v \cdot l} \Delta V_{GS} \tag{3.1}$$

where g_{m} is the transconductance, v is the electron drift velocity, l is the HEMT width, and ΔV_{GS} is the AC component of the applied gate-source voltage. The electron drift velocity (v = 0.4×10^7 cm/s) can be obtained from the calculated velocity-field curves for the measured electron density [51] with known electric field E = 1.43 MV/m (the horizontal field applied by the DC drain/source bias along the channel). The strain $\Delta\gamma_{\mathrm{zz}}$ can then be used to calculate the change in the index of refraction Δn_1 in GaN for transverse electric polarization through

$$\Delta n_1 = -0.5\, n_1^3\, p_{13}\, \Delta\gamma_{ZZ} \tag{3.2}$$

where p_{13} = 0.006 is the photoelastic constant for GaN [52] and n_1 = 2.33 is the GaN index of refraction at the HeNe laser wavelength [53]. The change in the normalized intensity of the reflected beam can be calculated as:

$$\frac{\Delta R}{R_0} = \frac{\left(n_1 + \Delta n_1 - n_0\right)^2}{\left(n_1 + \Delta n_1 + n_0\right)^2} - \frac{\left(n_1 - n_0\right)^2}{\left(n_1 + n_0\right)^2} \tag{3.3}$$

where n_0 = 1.00 is the index of refraction of air. Given the measured average reflected optical power (R_0 = 0.25 mW), the photodetector responsivity (0.4 A/W), and the integrated transimpedance amplifier gain (5×10^4 V/W), the voltage of the detected SAW signal can be predicted by this model and is shown in Figure 3-8b. The good match between model and measurement of strain-induced changes in optical reflectance suggests that modulated strain at various bias points can be accurately predicted based on known HEMT DC characteristics.

Using Equation 3.1, we can directly calculate the vertical strain modulation of the HEMT (~60 μm in length) characterized in Figure 3-8b; the result is shown in Figure 3-9. For comparison, the calculated strain modulation for the measured 50-pair IDT (which has the same width as the HEMT and is on the same AlGaN/GaN layer structure) is also shown, as well the responses of a three-pair IDT (60 μm long and hence the same chip area as the HEMT) and one-pair IDT (20 μm long), the latter two being derived using a scale factor to account for the fact that SAW strength in a multifinger IDT is proportional to the square of the number of electrode pairs [28]. The modulated strain magnitudes of both are consistent with the predictions given above based on Equations 1.1 and 1.2, and

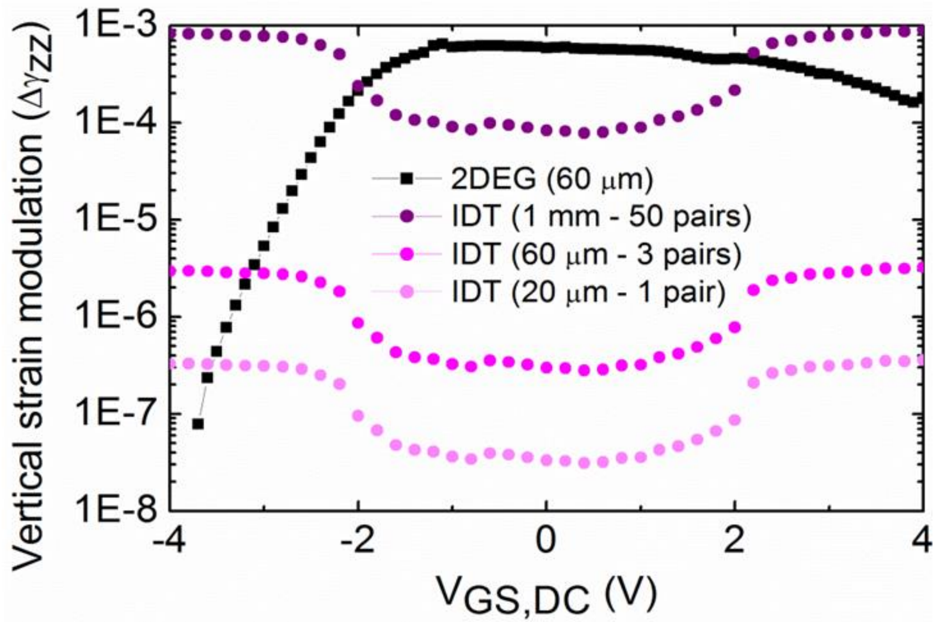

Figure 3-9: Calculated vertical strain modulation induced in the 2DEG by carrier density modulation, as a function of $V_{GS,DC}$, as well as the calculated vertical strain modulation induced by IDTs of three different sizes.

confirm that the HEMT provides strain modulation that is between two and three orders of magnitude greater than that of an IDT of the same chip area.

3.3.3 Single-gate HEMT

SAWs emitted from a HEMT geometry that only has a single gate electrode were also studied. DC characteristics and transconductance of the 1-gate HEMT are shown in Figures 3-10a and 3-10b. The emission spectrum of Figure 3-10e, in which the device was under the same bias conditions as the 4-gate transistor, shows four SAW modes: 460 MHz (R), 550 MHz (L), 760 MHz (PB1) and 990 MHz (PB2). The DC dependences of

the four SAW peaks are plotted in Figure 3-10c and show trends similar to those of the 4-gate HEMT plotted in Figure 3-8b.

The higher resonant frequencies of the 1-gate transistor suggest a shorter SAW wavelength; to investigate this, we held $V_{GS,DC}$ at 2 V and measured SAW spectra as V_{DS} was increased from 4 V to 12 V with 2 V steps, thus moving the channel's bias from the linear regime to saturation, as illustrated by the arrow and dots in Figure 3-10a. Figures 3-10d-h show that the R mode resonance shifts from 410 MHz to 470 MHz while the L mode resonance shifts from 510 MHz to 580 MHz as the channel shrinks in length due to pinch-off. This effect is further proof that the generation mechanism for the R and L modes is the dynamic modulation of the 2DEG. The R wave velocity is calculated as 4620 m/s from the 330 MHz resonance of the 4-gate device (which has a wavelength of 14 μm). Assuming the same R wave velocity, the wavelength in the 1-gate transistor is 11.3 μm in the linear regime (R peak at 410 MHz) and shrinks to 9.8 μm (the 2DEG's effective channel length) in the saturation regime (R peak at 470 MHz). Furthermore, this frequency shift is not observed in the 4-gate transistor geometry, as the wavelength is set by the periodicity of the multiple channels rather than the channel length. The resonant frequencies of the PB1 and PB2 modes are found to stay constant in both the 1-gate and 4-gate transistors, consistent with their generation by direct transduction of the RF signal rather than a process involving the 2DEG.

Finally, it should be noted that a 2DEG also provides a means for acoustic wave detection (as shown in Section 2.4), since a propagating acoustic mode causes a transient variation in its carrier density due to piezoelectric coupling [54]. In a biased 2DEG

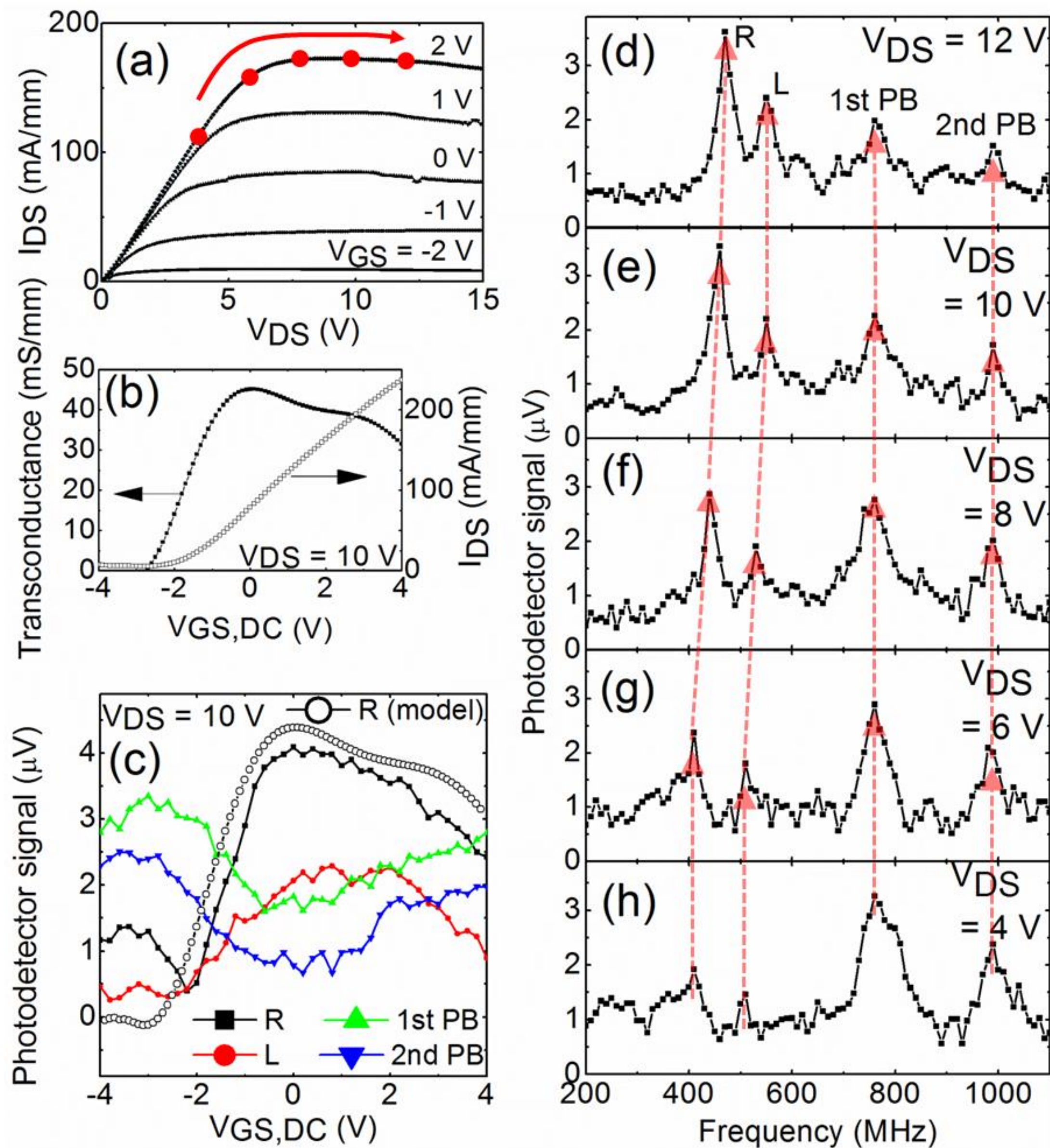

Figure 3-10: Characterization of the SAWs emitted by a single-gate HEMT. (a) DC characteristics of the 1-gate transistor. (b) Transconductance of the 1-gate transistor with V_{DS} set at 10 V. (c) DC dependences of the amplitudes of the four SAW modes emitted from the 2DEG as a function of $V_{GS,DC}$ when V_{DS} is set at 10 V. (d)–(h) Acoustic spectra when $V_{GS,DC}$ is set at 2 V and V_{DS} is increased in 2 V increments from 4 V to 12 V, as illustrated by the red dots and arrow in (a).

detector, this will lead to a transient signal in either its current or voltage characteristics (depending on the DC bias configuration of its terminals). Combined with the acoustic mode selectivity discussed above, a 2DEG-2DEG emitter-detector pair could therefore enable switchable multi-band applications.

3.4 Conclusion

In this chapter, we performed finite element analysis of the electrical fields in an AlGaN/GaN heterostructure under bias conditions in which the 2DEG is either depleted or present. The location of the most intense field modulation was found to occur at different depths in the epitaxy for different bias conditions, suggesting the ability to strongly transduce different SAW modes by varying the DC bias.

We then built an optical reflectance spectroscopy apparatus to measure the full SAW emission spectrum from a HEMT, including various SAW modes with different polarizations and penetration depths. Using this setup, we verified that a 2DEG SAW source is able to selectively turn on and off the emission of different acoustic modes based on applied DC bias conditions, leading to a unique functionality as a selective acoustic source. This technology can enable voltage-controlled acoustic emission at a specific depth and can furthermore provide a multi-band, amplified scheme for acoustic filtering and sensing applications.

In order to examine the impact of carrier flow on the emitted SAWs from a HEMT, the next chapter will present a detailed investigation of the interaction between emitted SAWs and electron drift current in a 2DEG.

Chapter 4

Coupling of SAWs and Drifting Electrons in a 2DEG

In previous chapters, we verified SAW emission from a modulated 2DEG and characterized the emission spectrum. It was shown that different SAW modes can be selectively emitted in a HEMT geometry by varying the gate-source DC bias.

One of the ways in which a 2DEG differs greatly from conventional transducers (e.g., IDTs) is that a 2DEG is highly electrically conducting whereas conventional transducers operate on insulating piezoelectric dielectrics. Based on acoustoelectric theory [18,19] developed decades ago for acoustic amplification in the presence of electrons with drift velocity higher than the acoustic phase velocity, we show below that a 2DEG can provide internally-amplified and uni-directional acoustic emission that is tuned by varying the drain-source voltage (which controls the electron drift velocity). For example, by simply switching the source-drain voltage polarity, one can switch the direction of emitted SAWs.

We first develop a model describing the amplification of SAWs by electron drift current in a 2DEG, and then experimentally examine directional SAW emission from a 2DEG.

4.1 Conventional Acoustoelectric Theory and Applications

Interactions between acoustic waves and electrons have been extensively studied for more than half a century. In 1953, the acoustoelectric effect was first theoretically described by Parmenter, who predicted that a travelling longitudinal acoustic wave could drive electrons to generate an electric current [55]. This effect was then thoroughly studied by many investigations in subsequent years [56-58].

In 1961, Hutson, McFee, and White demonstrated that bulk ultrasonic waves could be substantially amplified by drifting electrons if the electron velocity exceeds the speed of ultrasonic waves in CdS, a piezoelectric semiconductor [59]. Huston and White also developed a detailed analytic model describing the propagation of acoustic waves in a piezoelectric substrate and their amplification by drifting electrons [60, 61]. However, due to the low electron mobility in piezoelectric semiconductors at the time, it was common to use an applied voltage exceeding one kilovolt in order to move electrons faster than the ultrasonic waves. This posed serious problems for acoustoelectric devices, such as heating and degradation, which prevented further development [62].

Researchers soon realized that such problems could be largely mitigated by using surface acoustic waves (SAWs) instead of bulk ultrasonic waves. In addition, the invention by White and Voltmer of interdigital transducers (IDTs) in 1965 as efficient

and reliable SAW emitters [9] greatly accelerated research of the acoustoelectric effect involving SAWs. The experimental approaches for such studies involved depositing a semiconducting layer with high electron mobility on a piezoelectric substrate, or simply bringing a semiconducting slab close enough to a piezoelectric substrate that the air gap is less than one wavelength of the SAWs propagating in the piezoelectric substrate [63, 64]. The oscillating electric field excited by SAWs travelling in a piezoelectric substrate interacts with drifting electrons in the semiconductor layer, which can amplify (or attenuate) the SAWs if the electron drift velocity is higher (or lower) than the SAW velocity. This effect was extensively studied during the 1970s and 1980s with demonstrations of many varieties of acoustoelectric devices [14, 15, 65].

During the late 1980s, research in this area shifted to interactions between SAWs and two-dimensional electron gases (2DEGs) formed in GaAs/AlGaAs heterostructures rather than electrons in bulk materials. Attention was mostly focused on the attenuation of SAWs caused by a 2DEG. First, the attenuation of weak SAWs travelling over a 2DEG was studied [66, 67]; this occurs in the linear regime in which the conductive 2DEG screens the electric field accompanying the travelling SAWs. Because a 2DEG's conductivity can be easily characterized by measuring the attenuation of incident SAWs, such experiments provide a means to study the physics of low dimensional electrons, e.g., quantization of the Hall conductivity [68] or quantum oscillation [66]. Later, studies of intense SAWs incident on a 2DEG revealed a nonlinear effect [69] in which the 2DEG was broken into moving strips of electrons (electrons falling into the SAW potential minima) guided by SAWs with a large potential amplitude comparable to the semiconductor's band gap.

Recently, it was demonstrated that SAWs could be used to transport single electrons with maintained spins in a depleted 2DEG over macroscopic lengths at low temperatures [18, 19]. However, there has been no study in the literature on amplification of SAWs by electron drift in a 2DEG.

4.2 Amplification of Acoustic Waves by a Biased 2DEG

To quantify the amplification of SAWs by drifting electrons in a 2DEG, we first revisit the amplification of bulk acoustic waves by electron drift in a bulk piezoelectric semiconductor.

As a bulk wave propagates through a piezoelectric semiconductor, it induces a traveling sinusoidal potential that causes bunching of carriers and hence a periodic variation in electrical conductivity. In the presence of a DC current, this periodic conductivity leads to an additional periodic potential that has a phase difference with respect to the acoustic wave due to the motion of charge carriers. This phase difference leads to acoustic amplification under the condition that the electron drift velocity is higher than the acoustic wave speed.

The equations that describe piezoelectric coupling in a material can be written as:

$$T = cS - e_p E, \tag{4.1}$$

$$D = e_p S + \varepsilon E, \tag{4.2}$$

where c is the elastic constant at constant electric field, ε is the dielectric permittivity at constant strain, E is the electric field, T is the stress, e_p is the piezoelectric constant, and

D is the electric displacement. To derive the ultrasonic amplification coefficient [61], one first obtains an expression for the electric displacement, D, in terms of the E field from Poisson's equation and the current-density-space-charge continuity equation. This relation between D and E is then used to eliminate D from the equation 4.2, so that an expression for E in terms of the strain, S, is obtained, which is then substituted in the equation 4.1. The result is a complex elastic stiffness constant, c', which contains all of the electrical effects. The acoustic amplification coefficient, α, is then obtained from the imaginary part of $(c')^{-1/2}$, yielding [59]:

$$\alpha = k\frac{K^2}{2}\frac{(\omega_c/\omega\gamma)}{1+(\omega_c/\gamma\omega)^2(1+\omega^2/\omega_c\omega_D)^2} \tag{4.3}$$

where k is the acoustic wavenumber, ω is the acoustic frequency, $\omega_c = \sigma/\varepsilon$ is the conductivity relaxation frequency (for which σ is the conductivity and ε is the dielectric constants of the piezoelectric medium), $K^2 = e_p^2/c\varepsilon$ is the electromechanical coupling coefficient (for which e_p is the piezoelectric constant, and c is the stiffness constant), $\omega_D = v_S^2/D$ is the electron diffusion frequency (for which v_S is the acoustic velocity in the piezoelectric material, $D = \mu k_B T/e_0$ is the diffusion constant, μ is the electron mobility, k_B is the Boltzmann constant, T is absolute temperature, and e_0 is the electron charge), and $\gamma = v_d/v_S - 1$ is the dimensionless electron drift parameter (for which v_d is the electron drift velocity).

To modify Equation 4.3 to describe the interaction of SAWs with a 2DEG, an effective electromechanical coupling coefficient K_{eff}^2 is used which is slightly different

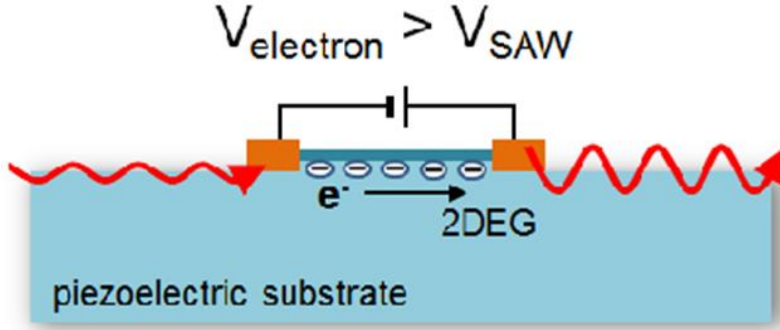

Figure 4-1: Illustration of a layer structure and applied bias supporting SAW amplification.

from the coefficient K^2 used for bulk waves [67]. Also, the conductivity relaxation frequency is replaced by the following 2D form [67]:

$$\omega_c = \sigma_S k / (\varepsilon_1 + \varepsilon_2), \tag{4.4}$$

where $\sigma_S = n_S e_0 \mu$ is the 2DEG sheet conductivity and n_S and μ are the 2DEG carrier density and electron mobility. Substituting into Equation 4.3 yields

$$\alpha = k \frac{K_{eff}^{\;2}}{2} \frac{\gamma (\sigma_S / \sigma_M)}{\gamma^2 + (\sigma_S / \sigma_M)^2 (1 + k\Lambda)^2}, \tag{4.5}$$

where $\Lambda = (\varepsilon_1 + \varepsilon_2) k_B T / e_0^2 n_S$ is the 2D screening length and $\sigma_M = v_S (\varepsilon_1 + \varepsilon_2)$. This is the governing equation for the interaction (amplification or attenuation) of SAWs by electron drift in a 2DEG. Figure 4-1 shows a layered structure supporting this interaction.

When an incident SAW travels over a 2DEG, the intensity of the SAW is increased if the electron drift velocity is larger than the SAW velocity ($\gamma > 0$).

Under the conditions of no electron drift ($\gamma = -1$) and a SAW wavelength much greater than the 2D electron screening length ($k\Lambda$ small), Equation 4.5 reverts to the well-known equation describing attenuation of SAWs by a 2DEG [67]:

$$\alpha = -k\frac{K_{eff}^{\ 2}}{2}\frac{(\sigma_S/\sigma_M)}{1+(\sigma_S/\sigma_M)^2}. \tag{4.6}$$

Furthermore, Equation 4.3 reverts to the 3D form (Equation 4.3) if Λ is replaced by kL_D^2,

where $L_D = \sqrt{\frac{\varepsilon_1 k_B T}{e_0^{\ 2} N_d}}$ is the 3D Debye screening length and N_d is the bulk carrier density.

The SAW power gain in decibels (dB) per unit length of interaction with drifting electrons in a 2DEG can be calculated in terms of the amplification coefficient derived in Equation 4.5:

$$G = 10\log_{10}\left[e^{-\alpha}\right]^2. \tag{4.6}$$

Figure 4-2 shows G as a function of electron drift velocity in a 2DEG for four different values of carrier density. Positive gain indicates that the SAW is amplified, while negative gain indicates attenuation. A positive electron velocity indicates that the SAW is travelling in the same direction as the drifting electrons, while negative indicates the opposite direction. The demonstrated strength of interaction in Figure 4-2 is calculated based on an $Al_{0.25}Ga_{0.75}N$/GaN 2DEG heterostructure grown on a sapphire substrate with an electron mobility of 1500 $cm^2/(V\cdot s)$ at 300 K. In this work, K^2 is used approximately

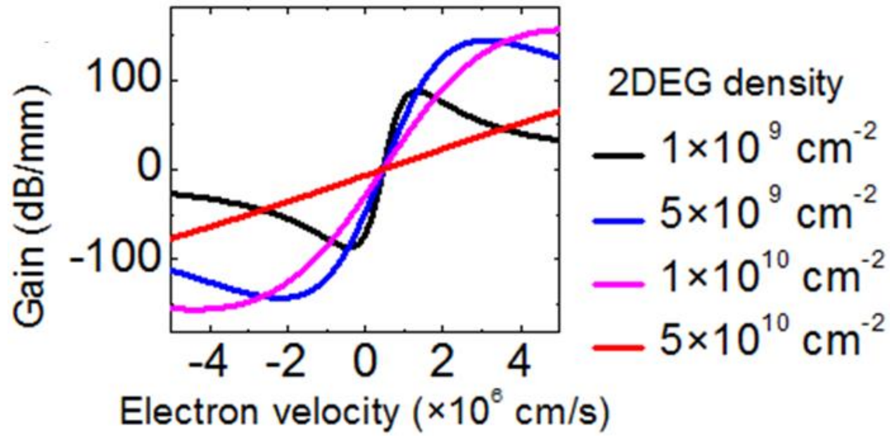

Figure 4-2: SAW power gain per unit length of interaction with a DC biased 2DEG, as a function of electron velocity for four different values of 2DEG carrier density.

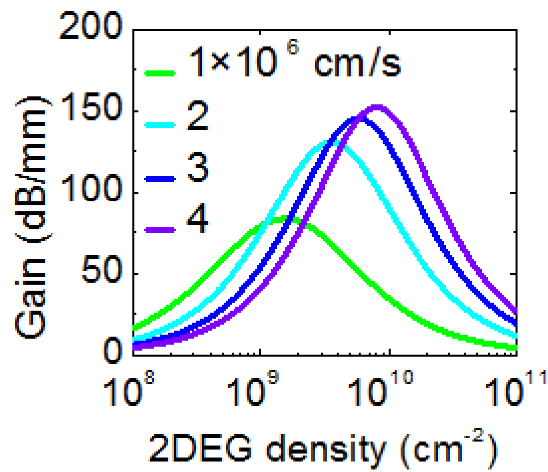

Figure 4-3: Gain per unit length as a function of 2DEG density for four different values of electron velocity, based on the same condition used in Figure 4-2.

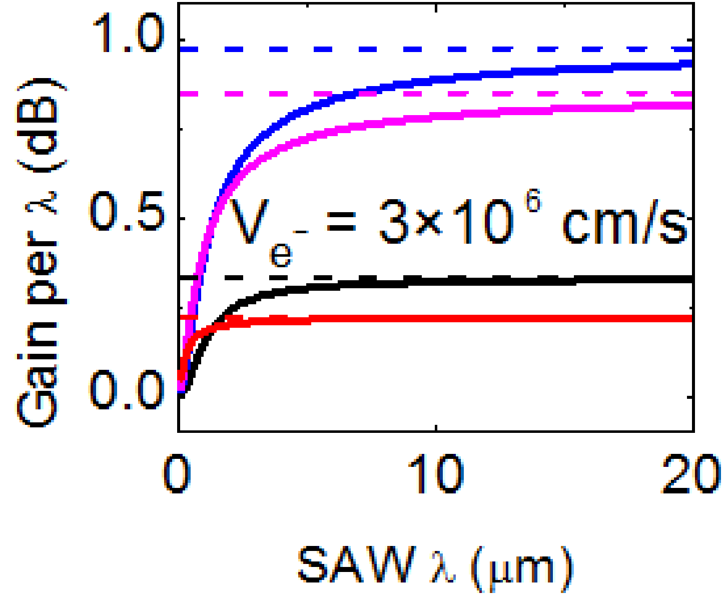

Figure 4-4: Solid curves: gain per SAW wavelength for the four different values of 2DEG density used in Figure 4-2, assuming an electron drift velocity of 3×10^6 cm/s; dashed curves: gain per SAW wavelength if electron diffusion is ignored by setting Λ to zero.

for K_{eff}^2 [67]. For this epitaxial structure, e_p = 1.14 C/m^2, c = 397 GPa [31], and ε_1 = 5.16ε_0 [70] at high frequencies (where ε_0 is the vacuum permittivity). The assumed frequency of the SAW is 0.8 GHz and its velocity is 4.6×10^5 cm/s, consistent with a 2 μm GaN on sapphire structure [33] that is used for experimental studies below. The crossover of G occurs when the electron velocity equals the SAW velocity.

Figure 4-3 shows G as a function of 2DEG density for four different values of electron velocity, based on the same layer structure used in Figure 4-2. The gain decreases after reaching its maximum as carrier density keeps increasing, because the

travelling piezoelectric field accompanying the SAW has a reduced bunching effect on local carrier density when this carrier density is high [61].

The solid lines in Figure 4-4 show the acoustic gain as a SAW travels by one wavelength through a 2DEG, for the four different values of 2DEG density used in Figure 4-2, while the electron drift velocity is set constant at 3×10^6 cm/s. The gain per wavelength drops quickly as the SAW wavelength decreases (SAW frequency increases) because the electrons cannot move fast enough to respond to the oscillating field generated by the travelling SAWs at high frequencies. This effect can be easily understood by ignoring the electron diffusion term in Equation 4.3 (setting Λ to zero), which leads to a constant gain per wavelength, as shown in the dashed lines.

Figure 4-5 compares the interaction of SAWs with drifting electrons in a bulk material and in a 2DEG. For bulk GaN at 300 K with an electron density between 10^{12} and 10^{18} cm^{-3} and a mobility of approximately 600 $cm^2/(V\cdot s)$ [71], the equivalent density in a 10-nm 2DEG quantum well formed at an AlGaN/GaN interface is between 10^6 and 10^{12} cm^{-2} and the mobility is approximately 1500 $cm^2/(V\cdot s)$. If the electron velocity is set constant at 3×10^6 cm/s, the maximum SAW gain produced by electron drift in bulk GaN is predicted to be 160 dB/mm, which is a little higher than that predicted for a GaN-based 2DEG (145 dB/mm). The former occurs at a smaller equivalent carrier density (~ 10^{14} cm^{-3}) than the latter (~ 10^{10} cm^{-2}), due to the 2DEG's higher effective resistance. Since a carrier density as low as 10^{14} cm^{-3} is difficult to obtain in bulk semiconductors due to unintentionally introduced impurities, while it is typical to obtain 10^{10} cm^{-2} in a 2DEG, a 2DEG could yield a higher maximum gain for practical carrier densities.

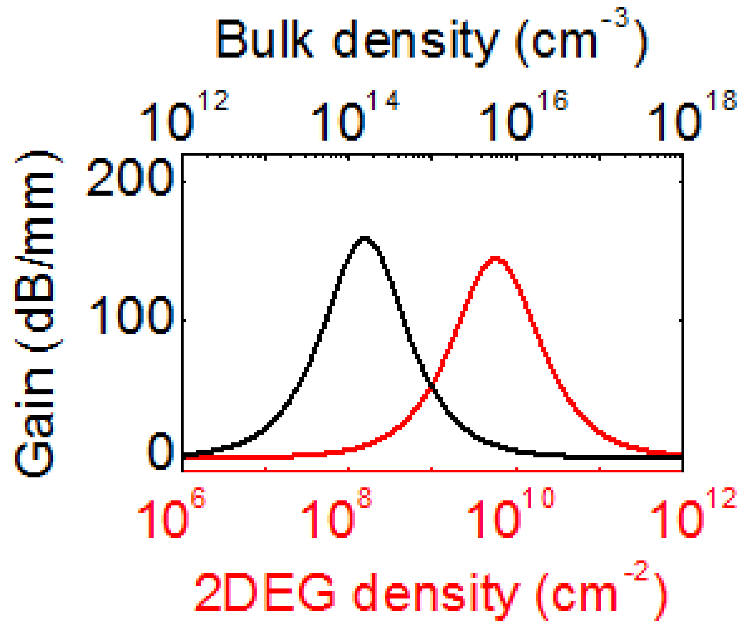

Figure 4-5: Comparison of the interaction strength for SAWs and drifting electrons in a GaN-based 2DEG and bulk GaN at equivalent carrier densities.

4.3 Characterizing Directional Emission of SAWs

The SAW-2DEG interaction allows a HEMT to not only emit SAWs by dynamic modulation of the carrier density [70, 72], but also to internally amplify (or attenuate) the emitted SAWs in particular directions. Figure 4-6 illustrates an experimental arrangement to investigate this phenomenon. An RF signal is applied across the source-gate (V_{GS}) to excite SAW emission in both drain-source and source-drain directions. Meanwhile, DC bias is applied across the drain-source (V_{DS}) to drive electron drift in the 2DEG channel which can, at certain bias conditions, substantially amplify the emitted SAWs propagating in one direction and attenuate those propagating in the other.

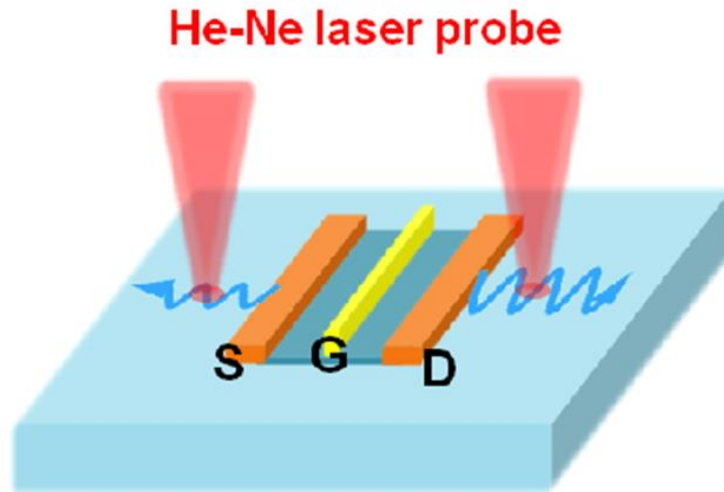

Figure 4-6: A HEMT on an AlGaN/GaN 2DEG structure is used as an active SAW emitter with directional emission functionality under certain bias conditions. S stands for source, G for gate, and D for drain.

Figure 4-7 shows the ratio of the SAW power emitted from the drain side to that from the source side, as a function of the electron drift velocity. This ratio is derived based on the gain per unit length from Figure 4-2, recognizing that SAWs emitted from the drain side interact with drifting electrons that have a positive velocity whereas SAWs emitted from the source side interact with drifting electrons that have a negative velocity. The SAW-2DEG interaction length is assumed to be one wavelength of the emitted SAW, which is also the effective channel length (given that the spacing of the modulated gate/source electrodes is approximately half of the channel length). This length used in Figure 4-7 is 6 μm, obtained from dividing the SAW velocity (4.6×10^5 cm/s) by the SAW frequency (0.8 GHz). The SAW power emitted from the drain side is found to be

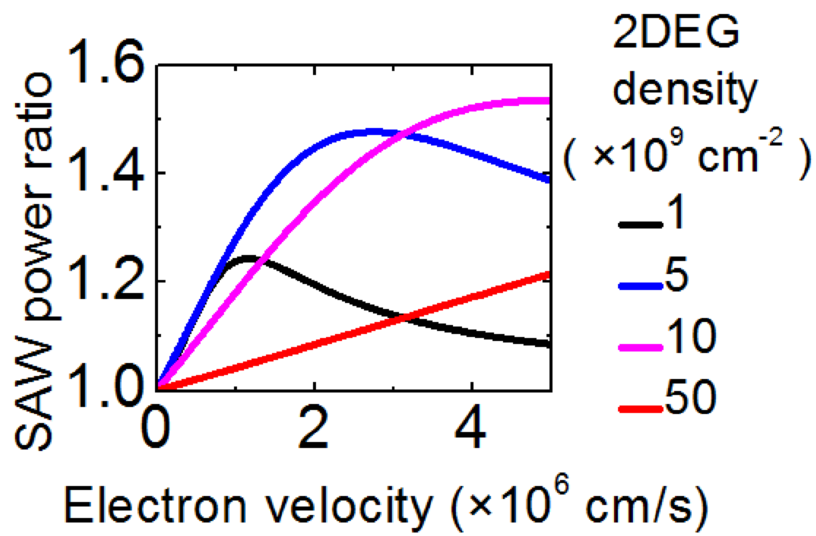

Figure 4-7: Calculated ratio of the SAW power emitted from the drain side to that from the source side as a function of electron velocity for four different values of 2DEG density.

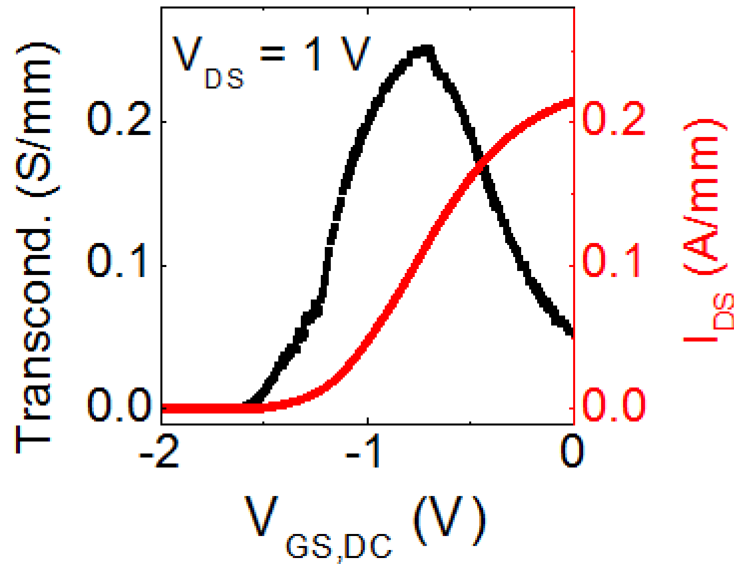

Figure 4-8: HEMT's transconductance and source-drain current (I_{DS}) as a function of V_{DS} and $V_{GS,DC}$, with V_{DS} held at 1 V.

nearly 1.6 times as large as that emitted from the source side at a 2DEG electron density of 1×10^{10} cm^{-2} and drift velocity of 4×10^{6} cm/s.

To experimentally investigate SAW amplification and consequent directional acoustic emission from a 2DEG, we studied a modified commercial GaN multi-gate high electron mobility transistor (HEMT) (Nitronex NPTB00050). The modification consisted of removing the sealing cap from the device package and using a micromanipulator-controlled Alessi probe needle to mechanically break all electrode interconnections except for one source, one gate, and one drain, forming a single-gate transistor structure. The source-drain spacing was 5.5 µm, and the layer structure was composed of 1.9 µm thick GaN-based epitaxy grown on a silicon substrate. Since sapphire and silicon have similar slow transverse acoustic velocities (5980 m/s in sapphire and 5842 m/s in silicon),

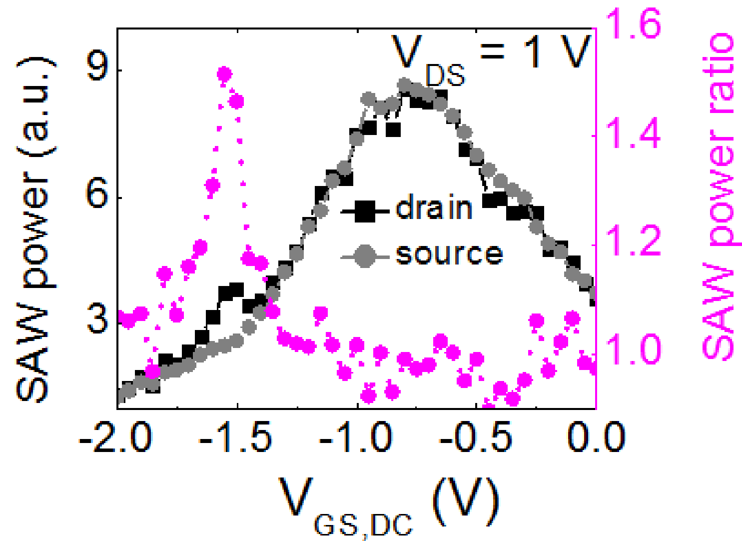

Figure 4-9: SAW power emitted at 0.8 GHz from the drain side (black) and source side (gray), as a function of $V_{GS,DC}$, with V_{DS} held at 1 V. The power is normalized to the minimum measured at $V_{GS,DC}$ = -2 V; the emission ratio (drain/source) is shown in magenta.

an approximate acoustic velocity of 4.6×10^5 cm/s was assumed based on the calculated velocity-thickness-wavelength dispersion relationship for a GaN/sapphire structure [33].

A HeNe laser was used as an optical probe [70] to measure SAW intensity by means of the photoelastic effect (see Section 3.2). The focused laser spot could be located precisely on either the drain side or source side to characterize the intensity of emitted SAWs in either direction. When an RF signal (80 mV_{P-P} at 0.8 GHz) was applied across V_{GS} at constant V_{DS} = 1 V, intense SAW emission was detected over a range of $V_{GS,DC}$ as shown in Figure 4-9. The applied RF power was small enough to ensure that the transduced piezoelectric potential amplitude was considerably less than the semiconductor's band gap, in order to prevent non-linear SAW-2DEG interactions from occurring.

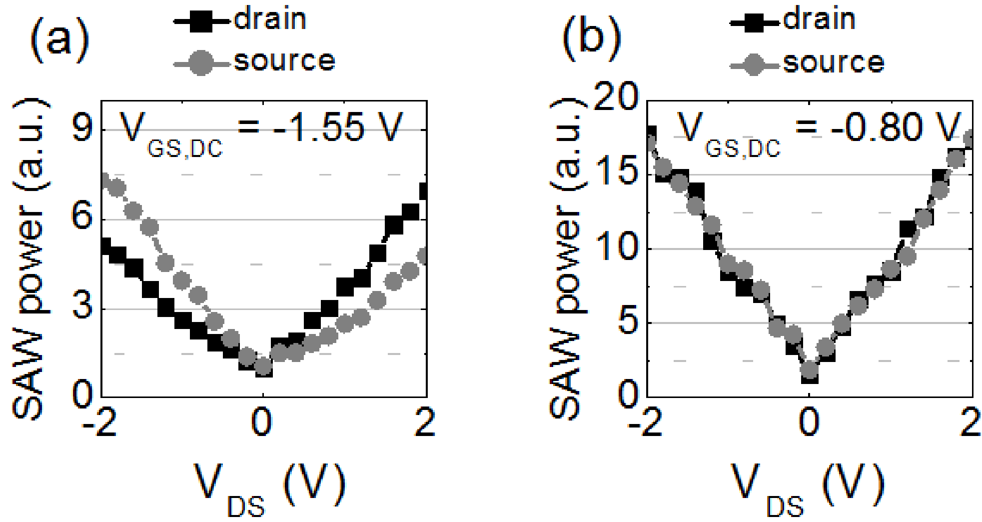

Figure 4-10: (a) and (b) SAW power emitted from the drain side and source side as a function of V_{DS}, with $V_{GS,DC}$ held at -1.55 V and -0.80 V, respectively.

The ratio of the measured power emitted from the drain side to that emitted from the source side reaches its peak near the threshold voltage of the transistor which is -1.55 V. For the applied electric field E = 1.82 kV/cm (corresponding to 1 V source-drain DC bias along the 5.5 μm channel), Monte Carlo simulations of electron-velocity-field characteristics [73] predict an electron drift velocity approximately 2.8×10^{6} cm/s. The 2DEG mobility is estimated to be approximately 1540 $cm^2/(V\cdot s)$ due to linear electron-velocity-field relationship at the low field region. Thus, from the estimated electron velocity and the 0.287 mA/mm current density near the peak SAW power ratio, the 2DEG density at this peak is estimated to be approximately 0.64×10^{10} cm^{-2}, consistent with the calculated maximum in Figure 4-3. The directional emission is smaller outside a small bias regime near threshold, due to reduced SAW-2DEG interaction under conditions of high carrier density. We also note here that the acoustoelectric effect could

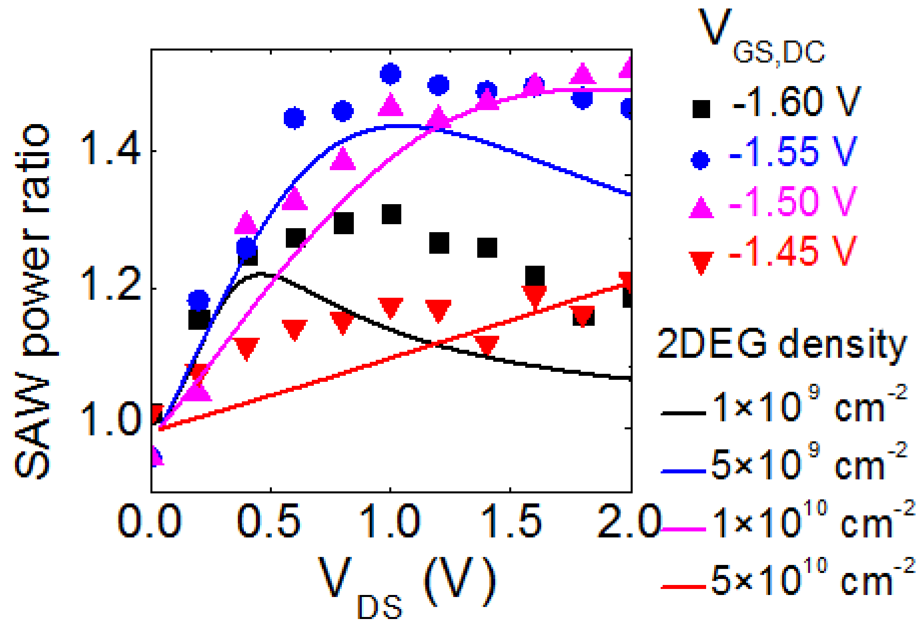

Figure 4-11: SAW power ratio (drain/source) as a function of V_{DS}, with $V_{GS,DC}$ varied from -1.60 V to -1.45 V with a step size of 0.05 V (points). Also shown are predicted power ratios for which the electron velocity in Figure 4-7 is converted to V_{DS} by assuming a constant 2DEG mobility (lines).

potentially be enhanced if the acoustic impedance profile were engineered to provide acoustic confinement within the 2DEG.

SAW emission was also measured while V_{DS} was varied from -2 V to 2 V and $V_{GS,DC}$ was held constant at -1.55 V or -0.80 V, as shown in Figures 4-10 (a) and (b), respectively. Figure 4-10 (a) clearly shows that the direction of SAW emission can be reversed by switching the direction of V_{DS}. Measured emitted power ratios at various V_{DS} and $V_{GS,DC}$ are shown as scattered points in Figure 4-11. The estimated carrier densities for the four bias voltages are 2.4, 6.4, 16, and 40×10^9 cm^{-2}. Also shown are solid lines generated from the model of Figure 4-7 under the assumptions of a constant electron

mobility of 1500 $cm^2/(V\cdot s)$ and a linear relationship between electron velocity and applied source-drain DC bias. The measurements and model match well for small source-drain voltage and deviate at high source-drain voltage as the relationship between electron velocity and applied field begins to deviate from linear relation. In addition, the calculated power ratio is based on carrier densities that are slightly different from the estimated densities.

4.4 Conclusion

We developed an analytic model describing the amplification of SAWs by electron drift current in a 2DEG. We then verified that SAWs emitted from an active HEMT-based acoustic emitter can be internally amplified (or attenuated) by drifting electrons under certain bias conditions, leading to a DC voltage tunable radiation pattern for acoustic emission.

Chapter 5

Conclusion and Future Work

The work presented here is a study of the performance and fundamental operating principles of active SAW emitters based on HEMT structures.

We first verified the emission of SAWs from a modulated AlGaN/GaN HEMT by fabricating integrated IDTs which have geometries that are resonant with that of the HEMT. HEMT-to-IDT transmission was characterized to demonstrate the strong emission of SAWs from the HEMT's 2DEG channel as a result of dynamic relaxation of the built-in strain in the AlGaN layer upon modulation of the 2DEG carrier density. Because 2DEGs have a very concentrated built-in piezoelectric field (~10 nm vs. ~10 μm in IDTs), they represent a source of very intense SAWs, which are increasingly desired in applications. 2DEGs were also demonstrated to detect incident SAWs due to dynamic strain modulation of their carrier density. Thus, a HEMT may enable high-speed, amplified detection of SAWs for sensing applications, and a 2DEG-2DEG emitter-detector pair could enable increased performance relative to existing SAW filter applications.

Because IDTs can only detect SAWs that are resonant with their designed geometries, we used optical reflectance spectroscopy to measure the full SAW emission spectrum from a HEMT, including various SAW modes with different polarizations and penetration depths. We demonstrated that a 2DEG SAW source is able to selectively turn on and off the emission of different acoustic modes based on applied bias conditions, leading to a unique selective acoustic source functionality.

We then investigated how charge carrier flow in a 2DEG impacts SAW emission. An analytic model describing SAW amplification and attenuation by electron drift current in a 2DEG was developed, and the emitted SAW intensity was predicted to be stronger in the direction of electron drift if the average electron velocity exceeds the SAW velocity. We then verified this directional emission by measuring emitted SAW power at the drain and source using optical reflectance microscopy. We found that the preferential direction of emission could be switched by switching the polarity of the applied drain-source bias voltage.

5.1 Future Work: Nondestructive Ultrasonic Diagnostics of HEMTs

In high-power and high-speed RF and microwave applications of HEMTs, material degradation due to thermal [39] and acoustic [40, 41] stresses can pose a significant problem, prompting studies of device reliability [42]. SAWs emitted by a HEMT could provide a means to nondestructively sample the degradation of its epitaxy and 2DEG in real time, since SAW propagation is known to depend strongly on crystal quality [11].

Because bulk GaN substrates are difficult to obtain due to cost and restrictions on wafer dimensions, GaN-based epitaxial structures are usually grown on substrates such as sapphire, silicon, and silicon carbide. Due to lattice mismatch between GaN and these substrates, the quality of the epitaxy near the GaN/substrate interface is usually very poor, and a large number of cracks and dislocations can be easily observed under microscopy. During high voltage operation of GaN HEMTs, a large mechanical strain is generated in the device area due to the piezoelectric effect. This strain is concentrated locally at cracks and dislocations, leading to deterioration of the epitaxy near the GaN/substrate interface. It has already been reported that HEMTs suffer sudden failures because of this effect [40].

In order to study this failure mechanism, an integrated IDT (with a geometry resonant with that of the HEMT) could be used for ultrasonic diagnostics by switching the HEMT to a bias condition in which strong SAWs are generated and then using the integrated IDT to characterize the HEMT's emitted SAW spectrum. By measuring changes in the emitted SAWs (e.g., peak frequency, peak amplitude, peak width, peak shape, etc.) during a controlled degradation study, the relationships between emitted SAW spectrum and device degradation could be obtained. Such a study could provide a basis for real-time diagnostic indicators of impending HEMT failure while it is being used in an application.

5.2 Future Work: 2DEG Transducers

Because 2DEGs provide an interesting platform for intense interactions between electric charges and 1) strain, by piezoelectric coupling; 2) light, by photo-excitation; and 3)

polar molecules, by change in surface potential; they could enable applications such as ultra-high frequency SAW emission (Section 5.2.1), high performance nanomechanical resonators (Section 5.2.2), and ultra-sensitive biomaterial detectors (Section 5.2.3).

5.2.1 GaN 2DEG-based Nanomechanical Resonators

Nanomechanical resonators such as free-standing membranes, cantilevers, doubly clamped beams, and suspended guitar-string-like nanotubes have recently attracted a great deal of attention because they provide a macroscopic platform to study coupling between mechanical excitations and elementary excitations such as quantum states [74], qubits (quantum analogue of the classical bit) [75], and single electrons [76]. Furthermore, they could have applications in fields as diverse as ultrasensitive mass detection [77], radio-frequency signal processing [78], mechanical logic circuits [79], and phonon lasing [80].

Furthermore, nanomechanical resonators are promising candidates for gigahertz (GHz) CMOS integrated on-die timing applications, potentially replacing the bulky off-chip quartz resonators which are used in most electronics today [81]. However, in continued efforts to scale down the size of mechanical resonators, capacitive feed-through presents a problem by inducing huge losses in measuring mechanical motion by a sensing transducer at multi-GHz frequencies. To improve the sensing signal-to-noise ratio, recent work has developed a resonant body transistor by integrating a sense transistor directly into the resonant body of a capacitively transduced silicon resonator [81]. Similarly, another study recently developed GaN-based resonant body transistors by

integrating a HEMT as a sense transistor directly on a suspended AlGaN/GaN membrane

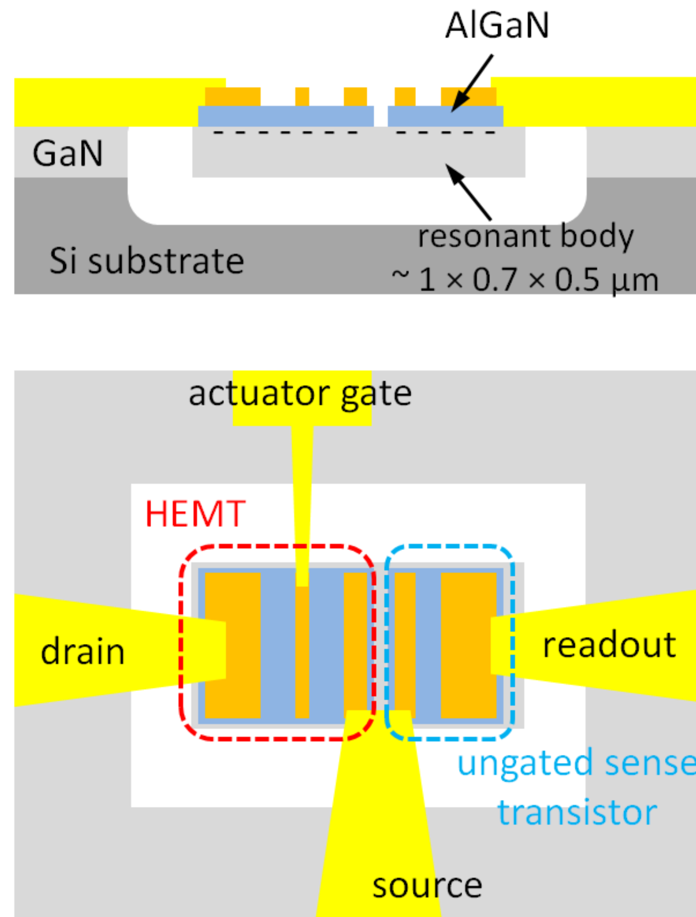

Figure 5-1: High electron mobility resonant body transistor. Dashed lines represent the 2DEG at the AlGaN/GaN interface.

as a means to increase the sensing signal due to the amplification provided by the HEMT [82]. However, the large capacitance of the actuator formed by the metal gate (top electrode) and 2DEG (bottom electrode) introduced loss in generating oscillation at high frequencies.

A suspended GaN HEMT rather than a 2-terminal transducer could provide a means for intense actuation at multi-GHz frequencies (see Figure 5-2). As described in

Section 2.3.1, by modulating the carrier density in the 2DEG of a GaN HEMT, large dynamic strains can be generate near the 2DEG due to piezoelectric coupling. Since the potential drop is concentrated at a 2DEG which has a thickness of only several nanometers, the field modulation across a 2DEG is extremely large, leading to intense dynamic strain generation, as verified in Section 3.3.2. While one HEMT under RF modulation is used to generate intense high frequency strains, the other HEMT which is ungated could be used as a sense transistor. Because transistors usually can be scaled well, a sub-micrometer size suspended resonant body HEMT-to-HEMT pair could provide a high-frequency nanomechanical resonator with promising quality factor (high Q).

5.2.2 GaN 2DEG-based Ultra-sensitive Bio-detectors

Figure 5-3a shows a typical HEMT design consisting of three electrodes: gate, source and drain. For a "normally on HEMT", when the gate is left unconnected, the 2DEG channel is filled with a great number of electrons and is highly conductive. Electrons drift from the source to the drain through the 2DEG channel when a DC voltage is applied across the source and drain electrodes. On the other hand, electrons in the 2DEG can be depleted by a negative gate-source voltage, leading to a highly resistant 2DEG channel. In this case, the HEMT is turned off.

GaN HEMT based biosensors could be used for rapid early detection of specific cancer antigens before costly and time-consuming clinical tests. A number of different electrical measurement approaches for biological materials have been studied extensively, although all of them have limitations. Electrochemical impedance measurements [83] are

inexpensive but suffer low sensitivity issues, whereas extremely sensitive antibody coated microcantilevers [84] and nanowire field effect transistors [85] are limited by an expensive fabrication process.

GaN HEMT based sensors have been found to be effective and potentially economical for scale-up, in addition to other advantages such as stability in harsh chemical environments. Prior work has demonstrated the excellent sensitivity and robustness of ungated AlGaN/GaN HEMTs because of their large changes in electrical current upon exposing the functionalized gate region to polar molecules, leading to applications in detecting gases, ions, pH values, proteins, and DNA [86-89]. This modulation of the HEMT current is due to the induced change in surface potential of the AlGaN barrier layer on top of the 2DEG by target molecules.

To improve the sensitivity of detecting tiny amount of cancer antigens in human blood, the thickness of the barrier layer on top of the 2DEG must be shrunk to several nanometers, instead of an AlGaN layer that is usually as thick as 20 nm (as shown in Figure 5-3b). This can be made possible by recent progress in nitride growth technology of an ultra-thin barrier layer AlInN/GaN structure which has been developed for terahertz microwave applications. AlInN/GaN-on-silicon wafers with AlInN layers that are only 4 nm are readily available. Furthermore, whereas most demonstrated GaN HEMTs have normally-on (depletion mode) characteristics, enormous efforts have been made recently to develop a normally-off GaN HEMT in high-power switching systems to prevent device destruction when the gate voltage becomes zero. Numerous schemes are available in the literature, such as gate recess [90], fluoride ion treatment [91, 92], and metal-oxide-semiconductor junction [93]. Such a normally-off structure is indispensable for ungated

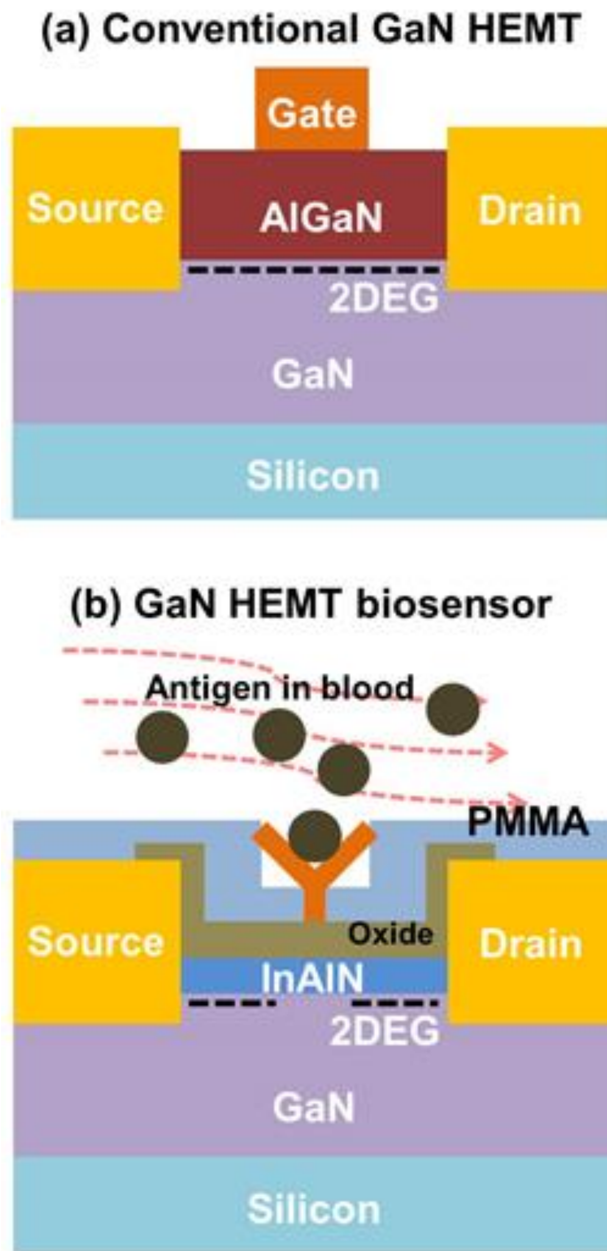

Figure 5-2: (a) Conventional AlGaN/GaN HEMT design. (b) Design of an InAlN/GaN HEMT based biosensor with a specially functionalized gate.

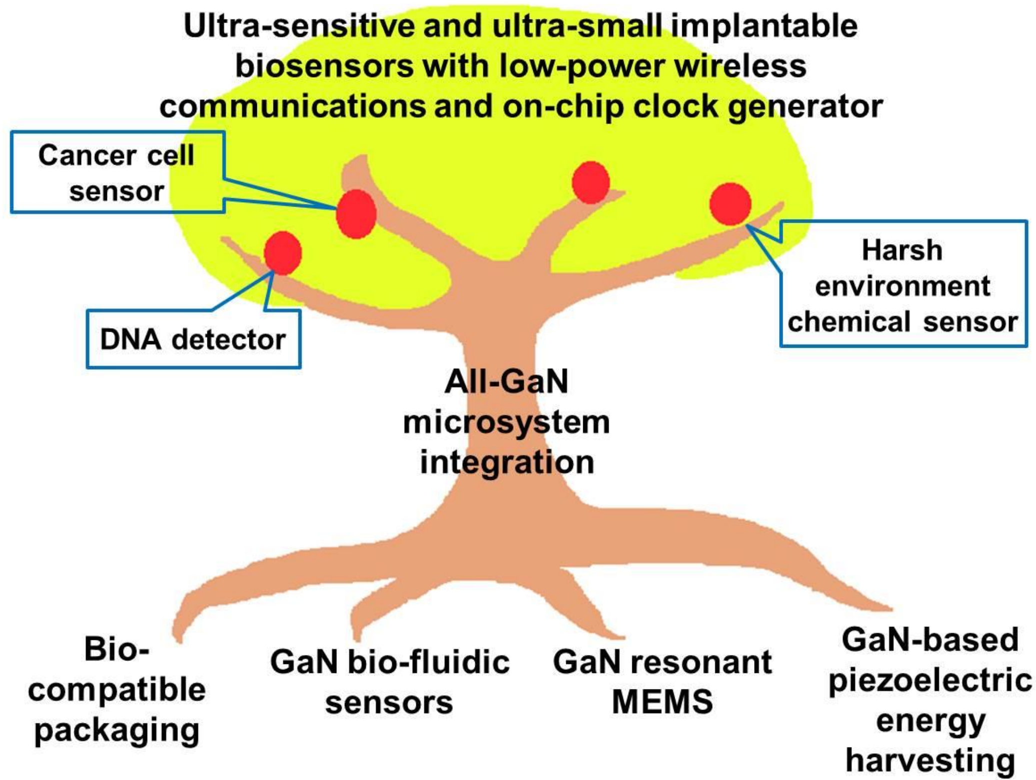

Figure 5-3: Vision for all-GaN-based biomedical and chemical sensing microsystems.

HEMT biosensors, because the current is desired to be zero for a device implanted in the human body for safety considerations and battery lifetime. This will be potentially a new paradigm for rapid detection of cancer antigens, while other devices are also possible, such as implantable blood pH sensors, remote harsh environment chemical sensors, etc.

The ultimate goal is to develop all-GaN-based ultra-sensitive low-power wireless biomedical sensing microsystems (depicted as a tree canopy in Figure 5-4) which consist of all-GaN-based building blocks such as bio-microfluidic devices, implantable biomedical sensors as described in this section, low-power wireless communication

devices, resonant MEMS for on-chip microprocessor clocking (described in Section 5.2.2), and GaN-based energy harvesting devices.

5.3 Pulsed Laser Interferometer

In the work presented here, optical reflectance spectroscopy was used to measure the dynamic strain associated with SAWs by means of the photoelastic effect. Although such a setup is relatively easy to build and calibrate, the photoelastic constants are not easy to obtain for some materials, and it is therefore difficult to compare measured vibrations among different types of materials.

In order to accurately characterize devices such as acoustic wave emitters and nanomechanical resonators, it is important to precisely measure their displacements. Optical interferometry is among the most sensitive measurement techniques and is well established for the transduction of nanomechanical displacements. For example, Michelson interferometers have been used for decades to measure small vibrational displacements and acoustic waves [94].

The standard Michelson interferometer setup includes a beam splitter to divide a CW laser into a signal arm and a reference arm. The former is reflected at the surface of the device under test, which modulates the total length of the signal arm due to the displacement being measured, whereas the latter is reflected by a fixed mirror. The two reflected laser beams are recombined at the same beam splitter and interfere with each other due to their optical path difference. A high-speed photodetector and spectrum analyzer are then used to obtain an electrical signal at the driven frequency of the

resonator. The amplitude of this detected RF signal can be used to derive the displacement. However, the Michelson interferometer is restricted to operating frequencies higher than 1 GHz because of the limited bandwidth of most photodetectors. In addition, optical interferometry involving a CW laser is only useful for frequency-domain characterization of vibrational modes.

A pulsed laser interferometer including a femtosecond laser probe with synchronized electrical excitation (either pulsed or sinusoidal) could provide a means for studying oscillating motion in the time domain at frequencies high than 10 GHz. For this setup (see Figure 5-5), the femtosecond laser pulse is used as the probe, while a synchronized reference sinusoidal signal from the controlling electronics of the laser is used as the pump. The pump signal is passed through a tunable electronic delay generator to control the relative timing between the sinusoidal excitation and probe pulse. The sinusoidal signal is then amplified and applied to the resonator. For lock-in detection, the output of the delay generator is chopped at a low frequency of several kilohertz. To form a Michelson interferometer for measuring dynamic displacements caused by excited acoustic resonances, the laser beam is divided into a signal arm and a reference arm by a polarized beam splitter. In the signal arm, the light is focused on the resonator using a long-working-distance microscope objective and then reflected back through the same objective. In the reference arm, the light is reflected by a fixed mirror and then re-combines with the light reflected from the resonator surface by the same beam splitter. The mirror is mounted on a precision piezoelectric stage to optimize the optical path difference for highest signal-to-noise ratio. These two combined reflected laser beams are then tuned to interfere with each other due to by the optical path difference modulated by

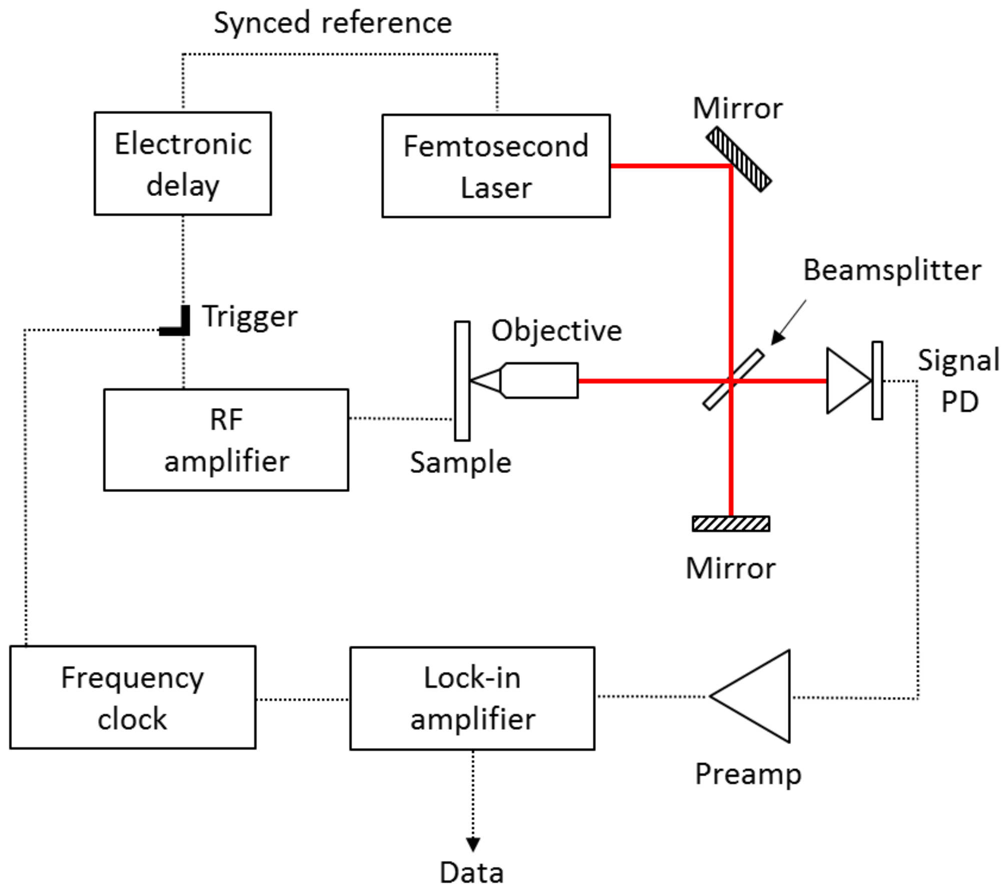

Figure 5-4: Stroboscopic Michelson interferometer (PD, photodiode). The beam path is indicated by red lines, while electrical connections are indicated by black dotted lines.

the displacement under measurement, and detected by a photodiode followed by a low-noise RF preamplifier and lock-in amplifier. The resonator's displacements can then be derived from the signal measured by the lock-in amplifier.

This stroboscopic Michelson interferometer could provide a number of benefits. First, since it uses a Michelson interferometer, this setup could be applicable to all devices, not just those designed as optical cavities. Second, it enables investigation of the time-domain response of a nanomechanical resonator subjected to sinusoidal electrical excitations, which could provide insight into device physics at its fundamental and higher harmonic resonant frequencies exceeding 10 GHz, etc. Finally, because the photodiode only needs to work at the frequency of the lock-in amplifier, the bandwidth of such an interferometer could be practically much greater than 1 GHz, and might only be limited by the trigger between the electronic delay and the RF amplifier and by the stray capacitance of the electrical connections.

Bibliography

[1] Copyright © 2005-2010, A.C. Akhavan.

[2] Y. V. Gulyaev, "Joint scientific session of the Physical Sciences Division of the Russian Academy of Sciences and the Joint Physical Society of the Russian Federation "Acoustoelectronics" - (30 March 2005)," *Physics-Uspekhi,* vol. 48, pp. 847-863, Aug 2005.

[3] J. Curie and P. Curie, "Développement par compression de l'électricité polaire dans les cristaux hémièdres à faces inclinées," *Bulletin de la Société minérologique de France,* vol. 3, pp. 90-93, 1880.

[4] D. A. Skoog, F. J. Holler, and S. R. Crouch, *Principles of instrumental analysis*, 6th ed. Belmont, CA: Thomson Brooks/Cole, 2007.

[5] "Market Report: World Piezoelectric Device Market". Acmite Market Intelligence, 2011.

[6] "Piezoelectric Actuators and Motors - Types, Applications, New Developments, Industry Structure and Global Markets". iRAP, Inc., ET119, 2013.

[7] R. C. Ruby, P. Bradley, Y. Oshmyansky, A. Chien, and J. D. Larson, "Thin film bulk wave acoustic resonators (FBAR) for wireless applications," *2001 Ieee Ultrasonics Symposium Proceedings, Vols 1 and 2,* pp. 813-821, 2001.

[8] D. Royer and E. Dieulesaint, *Elastic waves in solids*. Berlin ; New York: Springer, 2000.

[9] R. M. White and F. W. Voltmer, "Direct Piezoelectric Coupling to Surface Elastic Waves," *Applied Physics Letters,* vol. 7, pp. 314-&, 1965.

[10] M. Platshon, "Acoustic Touch Technology Adds a New Input Dimension," *Computer Design,* vol. 27, pp. 89-93, Mar 15 1988.

[11] D. Schneider and M. D. Tucker, "Non-destructive characterization and evaluation of thin films by laser-induced ultrasonic surface waves," *Thin Solid Films,* vol. 290, pp. 305-311, Dec 15 1996.

[12] E. R. Benes, R. Groschl, F. Seifert, and A. Pohl, "Comparison between BAW and SAW sensor principles," *Ieee Transactions on Ultrasonics Ferroelectrics and Frequency Control,* vol. 45, pp. 1314-1330, Sep 1998.

[13] R. Weigel, D. P. Morgan, J. M. Owens, A. Ballato, K. M. Lakin, K. Hashimoto*, et al.*, "Microwave acoustic materials, devices, and applications," *Ieee Transactions on Microwave Theory and Techniques,* vol. 50, pp. 738-749, Mar 2002.

[14] M. Luukkala and G. S. Kino, "Convolution and Time Inversion Using Parametric Interactions of Acoustic Surface Waves," *Applied Physics Letters,* vol. 18, pp. 393-&, 1971.

[15] P. Das, W. C. Wang, and M. N. Araghi, "Convolution of Signals Using Surface-Wave Delay-Lines," *Applied Physics Letters,* vol. 21, pp. 152-&, 1972.

[16] L. Y. Yeo and J. R. Friend, "Ultrafast microfluidics using surface acoustic waves," *Biomicrofluidics,* vol. 3, Jan-Mar 2009.

[17] X. Y. Ding, S. C. S. Lin, B. Kiraly, H. J. Yue, S. X. Li, I. K. Chiang*, et al.*, "On-chip manipulation of single microparticles, cells, and organisms using surface acoustic waves," *Proceedings of the National Academy of Sciences of the United States of America,* vol. 109, pp. 11105-11109, Jul 10 2012.

[18] S. Hermelin, S. Takada, M. Yamamoto, S. Tarucha, A. D. Wieck, L. Saminadayar*, et al.*, "Electrons surfing on a sound wave as a platform for quantum optics with flying electrons," *Nature,* vol. 477, pp. 435-438, Sep 22 2011.

[19] R. P. G. McNeil, M. Kataoka, C. J. B. Ford, C. H. W. Barnes, D. Anderson, G. A. C. Jones*, et al.*, "On-demand single-electron transfer between distant quantum dots," *Nature,* vol. 477, pp. 439-442, Sep 22 2011.

[20] A. D. Bykhovski, B. L. Gelmont, and M. S. Shur, "Elastic strain relaxation and piezoeffect in GaN-AlN, GaN-AlGaN and GaN-InGaN superlattices," *Journal of Applied Physics,* vol. 81, pp. 6332-6338, May 1 1997.

[21] L. F. Eastman, V. Tilak, J. Smart, B. M. Green, E. M. Chumbes, R. Dimitrov*, et al.*, "Undoped AlGaN/GaN HEMTs for microwave power amplification," *Ieee Transactions on Electron Devices,* vol. 48, pp. 479-485, Mar 2001.

[22] Y. F. Wu, D. Kapolnek, J. P. Ibbetson, P. Parikh, B. P. Keller, and U. K. Mishra, "Very-high power density AlGaN/GaN HEMTs," *Ieee Transactions on Electron Devices,* vol. 48, pp. 586-590, Mar 2001.

[23] The GaN Initiative for Grid Application (GIGA) program led by the Department of Energy was kicked off in 2009.

[24] M. Zhang, P. Bhattacharya, and W. Guo, "InGaN/GaN self-organized quantum dot green light emitting diodes with reduced efficiency droop," *Applied Physics Letters,* vol. 97, Jul 5 2010.

[25] M. Zhang, A. Banerjee, C. S. Lee, J. M. Hinckley, and P. Bhattacharya, "A InGaN/GaN quantum dot green (lambda=524 nm) laser," *Applied Physics Letters,* vol. 98, May 30 2011.

[26] O. Ambacher, B. Foutz, J. Smart, J. R. Shealy, N. G. Weimann, K. Chu*, et al.*, "Two dimensional electron gases induced by spontaneous and piezoelectric polarization in undoped and doped AlGaN/GaN heterostructures," *Journal of Applied Physics,* vol. 87, pp. 334-344, Jan 1 2000.

[27] J. Pedros, F. Calle, J. Grajal, R. J. Jimenez Rioboo, Y. Takagaki, K. H. Ploog*, et al.*, "Anisotropy-induced polarization mixture of surface acoustic waves in GaN/c-sapphire heterostructures," *Physical Review B,* vol. 72, Aug 2005.

[28] C. Campbell, *Surface acoustic wave devices for mobile and wireless communications*. San Diego: Academic Press, 1998.

[29] V. Fuflyigin, A. Osinsky, F. Wang, P. Vakhutinsky, and P. Norris, "Growth of ferroelectric oxide films on n-GaN/c-sapphire structures," *Applied Physics Letters,* vol. 76, pp. 1612-1614, Mar 20 2000.

[30] W. Cao, S. Bhaskar, J. Li, and S. K. Dey, "Interfacial nanochemistry and electrical properties of Pb(Zr0.3Ti0.7)O-3 films on GaN/sapphire," *Thin Solid Films,* vol. 484, pp. 154-159, Jul 22 2005.

[31] B. Jogai, J. D. Albrecht, and E. Pan, "Effect of electromechanical coupling on the strain in AlGaN/GaN heterojunction field effect transistors," *Journal of Applied Physics,* vol. 94, pp. 3984-3989, Sep 15 2003.

[32] F. Bernardini, V. Fiorentini, and D. Vanderbilt, "Spontaneous polarization and piezoelectric constants of III-V nitrides," *Physical Review B,* vol. 56, pp. 10024-10027, Oct 15 1997.

[33] J. Pedros, F. Calle, J. Grajal, R. J. Jimenez Rioboo, Y. Takagaki, K. H. Ploog*, et al.*, "Anisotropy-induced polarization mixture of surface acoustic waves in GaN/c-sapphire heterostructures," *Physical Review B,* vol. 72, pp. 075306-&, Aug 2005.

[34] S. H. Lee, H. H. Jeong, S. B. Bae, H. C. Choi, J. H. Lee, and Y. H. Lee, "Epitaxially grown GaN thin-film SAW filter with high velocity and low insertion loss," *Ieee Transactions on Electron Devices,* vol. 48, pp. 524-529, Mar 2001.

[35] F. Calle, J. Pedros, T. Palacios, and J. Grajal, "Nitride-based surface acoustic wave devices and applications," *E-Mrs 2004 Fall Meeting Symposia C and F,* vol. 2, pp. 976-983, 2005.

[36] F. Calle, J. Grajal, and J. Pedros, "Active SAW devices on 2DEG heterostructures," *Electronics Letters,* vol. 40, pp. 1384-1386, Oct 14 2004.

[37] K. Y. Wong, W. C. W. Tang, K. M. Lau, and K. J. Chen, "Planar Integration of SAW Filter with HEMT on AlGaN/GaN Heterostructure Using Fluoride-based Plasma Treatment," *2006 Ieee Ultrasonics Symposium, Vols 1-5, Proceedings,* pp. 281-284, 2006.

[38] M. Faucher, B. Grimbert, Y. Cordier, N. Baron, A. Wilk, H. Lahreche*, et al.*, "Amplified piezoelectric transduction of nanoscale motion in gallium nitride electromechanical resonators," *Applied Physics Letters,* vol. 94, Jun 8 2009.

[39] T. Batten, J. W. Pomeroy, M. J. Uren, T. Martin, and M. Kuball, "Simultaneous measurement of temperature and thermal stress in AlGaN/GaN high electron mobility transistors using Raman scattering spectroscopy," *Journal of Applied Physics,* vol. 106, Nov 1 2009.

[40] J. A. del Alamo and J. Joh, "GaN HEMT reliability," *Microelectronics Reliability,* vol. 49, pp. 1200-1206, Sep-Nov 2009.

[41] A. Sarua, H. F. Ji, M. Kuball, M. J. Uren, T. Martin, K. J. Nash*, et al.*, "Piezoelectric strain in AlGaN/GaN heterostructure field-effect transistors under bias," *Applied Physics Letters,* vol. 88, Mar 6 2006.

[42] G. Meneghesso, G. Verzellesi, F. Danesin, F. Rampazzo, F. Zanon, A. Tazzoli*, et al.*, "Reliability of GaN high-electron-mobility transistors: State of the art and perspectives," *Ieee Transactions on Device and Materials Reliability,* vol. 8, pp. 332-343, Jun 2008.

[43] J. H. Song, Q. Zhang, W. Patterson, A. V. Nurmikko, M. J. Uren, K. P. Hilton*, et al.*, "Generation of coherent gigahertz acoustic phonons in AlGaN/GaN microwave field-effect transistors," *Applied Physics Letters,* vol. 83, pp. 1023-1025, Aug 4 2003.

[44] J. Pedros, F. Calle, R. Cuerdo, J. Grajal, and Z. Bougrioua, "Voltage tunable surface acoustic wave phase shifter on AlGaN/GaN," *Applied Physics Letters,* vol. 96, Mar 22 2010.

[45] I. L. Guy, S. Muensit, and E. M. Goldys, "Extensional piezoelectric coefficients of gallium nitride and aluminum nitride," *Applied Physics Letters,* vol. 75, pp. 4133-4135, Dec 27 1999.

[46] A. Sarua, H. Ji, J. W. Pomeroy, M. J. Uren, T. Martin, and M. Kuball, "Converse piezoelectric strain in undoped and Fe-doped AlGaN/GaN heterostructure field effect transistors studied by Raman scattering," *Semiconductor Science and Technology,* vol. 25, Aug 2 2010.

[47] F. Gao, "Degradation study of AIGaN/GaN HEMT through electro-thermo-mechanical calculations and thermo-reflectance measurements," S m, Massachusetts Institute of Technology, 2010.

[48] http://www.synopsys.com/Tools/TCAD/DeviceSimulation/Pages/SentaurusDevice.aspx

[49] P. V. Santos, "Acoustic field mapping on GaAs using microscopic reflectance and reflectance anisotropy," *Applied Physics Letters,* vol. 74, pp. 4002-4004, Jun 28 1999.

[50] U. K. Mishra and J. Singh, *Semiconductor device physics and design*. Dordrecht, The Netherlands: Springer, 2008.

[51] J. Khurgin, Y. J. Ding, and D. Jena, "Hot phonon effect on electron velocity saturation in GaN: A second look," *Applied Physics Letters,* vol. 91, Dec 17 2007.

[52] E. Kim, B. Lee, A. Nahhas, and H. K. Kim, "Thin-film-induced index change and channel waveguiding in epitaxial GaN films," *Applied Physics Letters,* vol. 77, pp. 1747-1749, Sep 18 2000.

[53] G. Yu, G. Wang, H. Ishikawa, M. Umeno, T. Soga, T. Egawa*, et al.*, "Optical properties of wurtzite structure GaN on sapphire around fundamental absorption edge (0.78-4.77 eV) by spectroscopic ellipsometry and the optical transmission method," *Applied Physics Letters,* vol. 70, pp. 3209-3211, Jun 16 1997.

[54] L. Shao, M. Zhang, A. Banerjee, P. Bhattacharya, and K. P. Pipe, "Emission and detection of surface acoustic waves by AlGaN/GaN high electron mobility transistors," *Applied Physics Letters,* vol. 99, Dec 12 2011.

[55] R. H. Parmenter, "The Acousto-Electric Effect," *Physical Review,* vol. 89, pp. 990-998, 1953.

[56] G. Weinreich and H. G. White, "Observation of the Acoustoelectric Effect," *Physical Review,* vol. 106, pp. 1104-1106, 1957.

[57] G. Weinreich, T. M. Sanders, and H. G. White, "Acoustoelectric Effect in N-Type Germanium," *Physical Review,* vol. 114, pp. 33-44, 1959.

[58] W. C. Wang, "Strong Acoustoelectric Effect in Cds," *Physical Review Letters,* vol. 9, pp. 443-&, 1962.

[59] A. R. Hutson, D. L. White, and J. H. Mcfee, "Ultrasonic Amplification in Cds," *Physical Review Letters,* vol. 7, pp. 237-&, 1961.

[60] A. R. Hutson and D. L. White, "Elastic Wave Propagation in Piezoelectric Semiconductors," *Journal of Applied Physics,* vol. 33, pp. 40-&, 1962.

[61] D. L. White, "Amplification of Ultrasonic Waves in Piezoelectric Semiconductors," *Journal of Applied Physics,* vol. 33, pp. 2547-&, 1962.

[62] Y. V. Gulyaev and F. S. Hickernell, "Acoustoelectronics: History, present state, and new ideas for a new era," *Acoustical Physics,* vol. 51, pp. 81-88, Jan-Feb 2005.

[63] J. H. Collins, K. M. Lakin, C. F. Quate, and H. J. Shaw, "Amplification of Acoustic Surface Waves with Adjacent Semiconductor and Piezoelectric Crystals," *Applied Physics Letters,* vol. 13, pp. 314-&, 1968.

[64] C. Fischler and S. Yando, "Amplification of Guided Elastic Waves in Piezoelectric Plates through Electrical Coupling to a Semiconductor," *Applied Physics Letters,* vol. 15, pp. 366-&, 1969.

[65] V. E. Ljamov, R. M. White, and T. A. Hsu, "Surface Elastic-Wave Velocity and Second-Harmonic Generation in an Elastically Nonlinear Medium," *Journal of Applied Physics,* vol. 43, pp. 800-&, 1972.

[66] A. Wixforth, J. P. Kotthaus, and G. Weimann, "Quantum Oscillations in the Surface Acoustic-Wave Attenuation Caused by a Two-Dimensional Electron-System," *Physical Review Letters,* vol. 56, pp. 2104-2106, May 12 1986.

[67] A. Wixforth, J. Scriba, M. Wassermeier, J. P. Kotthaus, G. Weimann, and W. Schlapp, "Surface Acoustic-Waves on Gaas Alxga1-Xas Heterostructures," *Physical Review B,* vol. 40, pp. 7874-7887, Oct 15 1989.

[68] A. L. Efros and Y. M. Galperin, "Quantization of the Acoustoelectric Current in a 2-Dimensional Electron-System in a Strong Magnetic-Field," *Physical Review Letters,* vol. 64, pp. 1959-1962, Apr 16 1990.

[69] M. Rotter, A. V. Kalameitsev, A. O. Govorov, W. Ruile, and A. Wixforth, "Charge conveyance and nonlinear acoustoelectric phenomena for intense surface acoustic waves on a semiconductor quantum well," *Physical Review Letters,* vol. 82, pp. 2171-2174, Mar 8 1999.

[70] L. Shao, M. Zhang, A. Banerjee, P. K. Bhattacharya, and K. P. Pipe, "Electrically driven nanoscale acoustic source based on a two-dimensional electron gas," *Applied Physics Letters,* vol. 103, pp. 083102-&, Aug 19 2013.

[71] V. W. L. Chin, T. L. Tansley, and T. Ostochan, "Electron Mobilities in Gallium, Indium, and Aluminum Nitrides," *Journal of Applied Physics,* vol. 75, pp. 7365-7372, Jun 1 1994.

[72] L. Shao, M. Zhang, A. Banerjee, P. Bhattacharya, and K. P. Pipe, "Emission and detection of surface acoustic waves by AlGaN/GaN high electron mobility transistors," *Applied Physics Letters,* vol. 99, pp. 243507-&, Dec 12 2011.

[73] L. Ardaravicius, A. Matulionis, J. Liberis, O. Kiprijanovic, M. Ramonas, L. F. Eastman*, et al.*, "Electron drift velocity in AlGaN/GaN channel at high electric fields," *Applied Physics Letters,* vol. 83, pp. 4038-4040, Nov 10 2003.

[74] T. Rocheleau, T. Ndukum, C. Macklin, J. B. Hertzberg, A. A. Clerk, and K. C. Schwab, "Preparation and detection of a mechanical resonator near the ground state of motion," *Nature,* vol. 463, pp. 72-75, Jan 7 2010.

[75] M. D. LaHaye, J. Suh, P. M. Echternach, K. C. Schwab, and M. L. Roukes, "Nanomechanical measurements of a superconducting qubit," *Nature,* vol. 459, pp. 960-964, Jun 18 2009.

[76] M. D. LaHaye, O. Buu, B. Camarota, and K. C. Schwab, "Approaching the quantum limit of a nanomechanical resonator," *Science,* vol. 304, pp. 74-77, Apr 2 2004.

[77] A. K. Naik, M. S. Hanay, W. K. Hiebert, X. L. Feng, and M. L. Roukes, "Towards single-molecule nanomechanical mass spectrometry," *Nature Nanotechnology,* vol. 4, pp. 445-450, Jul 2009.

[78] C. T. C. Nguyen, "Frequency-selective MEMS for miniaturized low-power communication devices," *Ieee Transactions on Microwave Theory And Techniques,* vol. 47, pp. 1486-1503, Aug 1999.

[79] I. Mahboob and H. Yamaguchi, "Bit storage and bit flip operations in an electromechanical oscillator," *Nature Nanotechnology,* vol. 3, pp. 275-279, May 2008.

[80] I. Mahboob, K. Nishiguchi, A. Fujiwara, and H. Yamaguchi, "Phonon Lasing in an Electromechanical Resonator," *Physical Review Letters,* vol. 110, Mar 18 2013.

[81] D. Weinstein and S. A. Bhave, "The Resonant Body Transistor," *Nano Letters,* vol. 10, pp. 1234-1237, Apr 2010.

[82] A. Ansari and M. Rais-Zadeh, "A Thickness-Mode AlGaN/GaN Resonant Body High Electron Mobility Transistor," *Ieee Transactions on Electron Devices,* vol. 61, pp. 1006-1013, Apr 2014.

[83] J. X. Wang, X. W. Sun, A. Wei, Y. Lei, X. P. Cai, C. M. Li*, et al.*, "Zinc oxide nanocomb biosensor for glucose detection," *Applied Physics Letters,* vol. 88, Jun 5 2006.

[84] K. S. Hwang, J. H. Lee, J. Park, D. S. Yoon, J. H. Park, and T. S. Kim, "In-situ quantitative analysis of a prostate-specific antigen (PSA) using a nanomechanical PZT cantilever," *Lab on a Chip,* vol. 4, pp. 547-552, 2004.

[85] G. F. Zheng, F. Patolsky, Y. Cui, W. U. Wang, and C. M. Lieber, "Multiplexed electrical detection of cancer markers with nanowire sensor arrays," *Nature Biotechnology,* vol. 23, pp. 1294-1301, Oct 2005.

[86] B. S. Kang, H. T. Wang, F. Ren, S. J. Pearton, T. E. Morey, D. M. Dennis*, et al.*, "Enzymatic glucose detection using ZnO nanorods on the gate region of AlGaN/GaN high electron mobility transistors," *Applied Physics Letters,* vol. 91, Dec 17 2007.

[87] H. T. Wang, B. S. Kang, F. Ren, S. J. Pearton, J. W. Johnson, P. Rajagopal*, et al.*, "Electrical detection of kidney injury molecule-1 with AlGaN/GaN high electron mobility transistors," *Applied Physics Letters,* vol. 91, Nov 26 2007.

[88] B. S. Kang, H. T. Wang, T. P. Lele, Y. Tseng, F. Ren, S. J. Pearton*, et al.*, "Prostate specific antigen detection using AlGaN/GaN high electron mobility transistors," *Applied Physics Letters,* vol. 91, Sep 10 2007.

[89] B. S. Kang, H. T. Wang, F. Ren, B. P. Gila, C. R. Abernathy, S. J. Pearton*, et al.*, "pH sensor using AlGaN/GaN high electron mobility transistors with Sc2O3 in the gate region," *Applied Physics Letters,* vol. 91, Jul 2 2007.

[90] W. Saito, Y. Takada, M. Kuraguchi, K. Tsuda, and I. Omura, "Recessed-gate structure approach toward normally off high-voltage AlGaN/GaN HEMT for power electronics applications," *Ieee Transactions on Electron Devices,* vol. 53, pp. 356-362, Feb 2006.

[91] Y. Cai, Y. G. Zhou, K. J. Chen, and K. M. Lau, "High-performance enhancement-mode AlGaN/GaN HEMTs using fluoride-based plasma treatment," *Ieee Electron Device Letters,* vol. 26, pp. 435-437, Jul 2005.

[92] Y. Cai, Y. Zhou, K. M. Lau, and K. J. Chen, "Control of threshold voltage of AlGaN/GaN HEMTs by fluoride-based plasma treatment: From depletion mode to enhancement mode," *Ieee Transactions on Electron Devices,* vol. 53, pp. 2207-2215, Sep 2006.

[93] H. Kambayashi, Y. Satoh, S. Ootomo, T. Kokawa, T. Nomura, S. Kato*, et al.*, "Over 100 A operation normally-off AlGaN/GaN hybrid MOS-HFET on Si substrate with high-breakdown voltage," *Solid-State Electronics,* vol. 54, pp. 660-664, Jun 2010.

[94] J. V. Knuuttila, P. T. Tikka, and M. M. Salomaa, "Scanning Michelson interferometer for imaging surface acoustic wave fields," *Optics Letters,* vol. 25, pp. 613-615, May 1 2000.